UNIVERSITÀ DEGLI STUDI DI PADOVA

DIPARTIMENTO DI INGEGNERIA INDUSTRIALE

Tesi di Laurea Magistrale in Ingegneria dei Materiali

EFFECTS OF HEAT TREATMENT AND COLD ROLLING ON KINETICS OF FERRITE DECOMPOSITION PROCESSES IN DDS 2507

Relatrice: Prof. Irene Calliari
Correlatore: Prof. Istvan Mészàros

Laureando: Angelo Todesco
Matricola: 1087090

ANNO ACCADEMICO 2015-2016

A mio papà

ABSTRACT

This thesis work is a study on the effects of previous cold rolling on the kinetics of ferrite decomposition process, especially the eutectic decomposition $\delta \rightarrow \gamma' + \sigma$ at four different heat treatment temperatures.

In this work 35 samples of DSS 2507 grade (UNS S32750) have been cold rolled at 6 different thicknesses 10% - 20% - 30% - 40% - 50% - 60% and after that have been heat treated for 1800s (30min) at 700°C – 750°C – 800°C – 850°C.

The microstructure has been characterized by optical microscopy (OM) and scanning electron microscopy (SEM) with EBSD technique. The amount of ferrite phase has been determined with magnetic tests such as Stäblein-Steinitz tester, Eddy Current tester and Fischer-Ferrite tester.

We noticed that there was not a phase transformation due to the cold rolled deformation, but after the heat treatment at 850°C a huge quantity of ferrite decomposed into σ-phase in all the samples and this aspect has been highly accentuated in the most deformed specimens.

For this reason we can affirm that the cold rolled deformation increases the amount of sigma phase that precipitate in the material.

Furthermore it seems that the sigma phase precipitation, which occurs mainly at the grain boundary, beginning within the ferrite grains themselves, but we need further investigation.

This work has been performed in Budapest at the BME - Budapesti Műszaki és Gazdaságtudományi Egyetem – university of Budapest, Department of Science and Engineering Materials under the guidance of Dott. Mészáros István and in collaboration with University of Miskolc and KFKI - Research Institute for particle and nuclear physics in Budapest.

CONTENTS

INTRODUCTION

Starting from 1940s there has been considerable advances in metallurgy processes and technologies which have extended their development and their applications in many fields such as oil / petrochemical, mining, energy, nuclear.
One of the most important products is the stainless steel, which are ferrous alloys with more than 10.5% Cr content. This kind of steel is important most of all for it's excellent corrosion resistance due to the passivity property in oxidized environment. This feature is related to the amount of chromium, which must be higher than 10.5%.
Stainless steels can be divided into four different categories depending on their microstructure and their ferrite-austenite ratio:

- Austenitic steel is characterized by it's austenitic phase witnessed at room temperature due to the high quantity of γ-former elements. They have high resistance to corrosion and their austenitic structure (FCC) make them immune to the ductile-brittle transition, hence, they keep their toughness down to cryogenic temperatures.
- Ferritic steel is characterized by BCC structure as carbon steel but the mechanical characteristics cannot be increased by heat treatments.
- Martensitic steel has very high mechanical characteristics and is the only stainless steel that can be subjected to quenching, a heat treatment adapted to increase the mechanical properties.
- Duplex steel is characterized by a mixed structure with a ferrite-austenite ratio near to 50-50%. This particular structure has a higher corrosion resistance and toughness than witnessed with ferritic steel.

This study is concerned with a particular type of duplex stainless steel, UNS S32507. Other thesis' and articles talked about that DSS after cold rolling show a transformation, in percentage, from ferritic phase into austenitic phase depending on the rate of the cold deformation. This aspect is vitally important because it changes the characteristics of the steel and has been verified in other duplex steel by previous studies such as Emilio Manfrin thesis.

The study continues with the application of 4 thermal treatments at different temperatures (700°C - 750°C - 800°C - 850°C) in order to analyze the decomposition of the ferrite phase. This process was performed to understand if there is a correlation between the deformation rate and the precipitation of the sigma phase in the ferrite decomposition.

A complete analysis with several magnetic tests was performed (Stäblein-Steinitz, Eddy Current, Fischer-Ferrite) and microstructure analysis by optical microscope and EBSD, which allowed to obtain useful phase maps for further investigations.

This entire study has been started and completed at the BME - Budapesti Műszaki és Gazdaságtudományi Egyetem – University of Budapest, Department of Science and Engineering Materials under the guidance of Dott. Mészáros István and PhD Bögre Bàlint.

CHAPTER 1

DUPLEX STAINLESS STEEL (DSS)

1.1 GENERAL ASPECTS

Duplex stainless steels (DSS) are a category of stainless steels, which have a biphasic microstructure consisting of ferritic and austenitic in approximately same proportions.

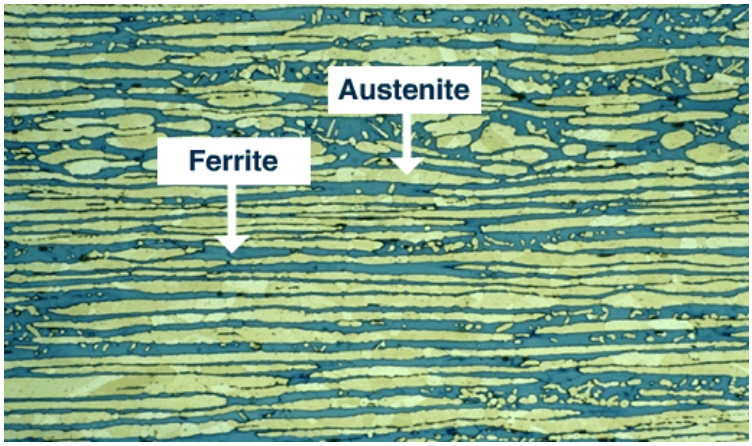

Fig 1. Duplex stainless steel microstructure

The picture in Fig 1. shows the yellow austenitic phase as grains surrounded by the blue ferritic phase. When duplex stainless steel is melted it solidifies from the liquid phase to a completely ferritic structure. As the material cools to room temperature, about half of the ferritic grains transform to austenitic grains ("islands"). The result is a microstructure of roughly 50% austenite and 50% ferrite.

DSS are characterized by high chromium percentage between 19% and 32% and molybdenum up to 5% and lower nickel contents than austenitic stainless steels.

The physical properties are a combination of the ferritic and the austenitic grades. In this way proprieties like high strength and an excellent resistance to corrosion made DSS very interesting for many purposes.

Due to their mixed microstructure, duplex stainless steels have roughly twice the strength compared to austenitic stainless steels and also improved resistance to localized corrosion, particularly pitting, and stress corrosion cracking (SCC). The properties of DSS are achieved with an overall lower alloy content than similar-performing super-austenitic grades, making their use cost-effective for many applications.

1.2 HISTORICAL ASPECTS

The first information recorded about DSS was at the beginning of 1930s. Bain and Griffith developed a two-phase stainless alloy in 1927[1]. The first commercial DSS, named 453E and whose chemical composition was about 25%Cr-5%Ni, seems to be made in 1929 by Avesta Jernverk[2].

Duplex stainless steels in cast form were produced in Scandinavian area, to be used in the sulfite paper industry [3]. The firsts industrial applications appeared between 1930 and 1940, either on die cast and on hot worked.

The mechanical characteristics and the wear resistance of this first "duplex stainless steel" have been improved. During the 1950s the introduction of the American regulation AISI 329 (25 Cr / 5 Ni / 1, 5 Mo) took place, and in the same years there was also the creation of the SANDVIK 3RE60 (18,5Cr / 5 Ni / 2,7 Mo), one of the precursor of the modern dual-phase stainless steels. In the 70's the industries began to use new refining technology such as vacuum and argon oxygen decarburization (VOD and AOD), which improved sensitively the quality and the mechanical features of stainless steels. In fact, the possibility to reduce the content of residual elements (like O_2, S, C, etc.) and at the same time obatain precise range of steel's composition, particularly for the nitrogen content, improve to have higher corrosion resistance and the high temperature behavior of stainless dual-phase steel. These manufacturing methods, together with the introduction of the continuous casting process, allowed for a significant reduction in production costs.

At the end of the 1970's we witnessed the development of a chemical

composition of stainless dual-phase steel with 22% of Cr and 5% of Ni, with also a small amount of nitrogen; this steel showed high mechanical resistance, it was weldable and was not effected by integranular corrosion. Due to the versatility and the very good performances there was a great diffusion of this steel among many users. The steel I refer to is the widespread and well known 2205 grade, one of the main two-phase stainless steels.

From 1980 there was a rapid diffusion of biphasic stainless steels called *superduplex*. The typical composition of these steels is: 25% Cr, 7% Ni and 3% Mo.

A market disposition took in these years a developed class of biphasic stainless steels low-alloy, which the mainly is the SANDVIK 2304, which can be considered competitive to the traditional austenitic stainless steels AISI 304 and 316 in the environments where required resistance to stress corrosion cracking and mechanical resistance.[4][5]

1.3 CLASSIFICATION

Duplex grades are characterized into groups based on their alloy content and corrosion resistance.

- ***Lean duplex*** refers to grades such as UNS S32101 (LDX 2101), S32202 (UR2202), S32304, and S32003.
- ***Standard duplex*** is 22% chromium with UNS S31803/S32205 known as 2205 being the most widely used.
- ***Super duplex*** is by definition a duplex stainless steel with a Pitting Resistance Equivalent Number (PREN) > 40, where PREN = %Cr + 3.3x(%Mo + 0.5x%W) + 16x%N. Usually super duplex grades have 25% chromium or more and some common examples are S32760 (Zeron 100 via Rolled Alloys), S32750 (2507) and S32550 (Ferralium).

- ***Hyper duplex*** refers to duplex grades with a PRE > 48 and at the moment only UNS S32707 and S33207 are available on the market.

Grade	UNS	EN	C	Cr	Ni	Mo	Mn	N	Cu	W
First generation DSSs										
329	S32900	1.4460	0.08	23.0-28.0	2.5-5.0	1.0-2.0	1.0	not-defined	23.0-28.0	2.5-5.0
3RE60	S31500	1.4417	0.03	18.0-19.0	4.3-5.2	2.5-3.0	1.2-2.0	0.05-0.10	18.0-19.0	4.3-5.2
UR50	S32404		0.04	20.5-22.5	5.5-8.5	2.0-3.0	2.0	–	1.00-2.00	–
Modern DSSs										
2304	S32304	1.4362	0.03	21.5-24.5	3.0-5.5	0.0-0.6	2.5	0.05-0.20	–	–
2205	S31803	1.4462	0.03	21.0-23.0	4.5-6.5	2.5-3.5	2.0	0.08-0.20	–	–
2205	S32205	1.4462	0.03	22.0-23.0	4.5-6.5	3.0-3.5	2.0	0.14-0.20	–	–
DP-3	S31260		0.03	24.0-26.0	5.5-7.5	5.5-7.5	1.0	0.10-0.30	0.20-0.80	0.10-0.50
UR52N	S32520	1.4507	0.03	24.0-26.0	5.5-8.0	3.0-5.0	1.5	0.20-0.35	0.50-3.00	–
255	S32550	1.4507	0.04	24.0-27.0	4.5-6.5	2.9-3.9	1.5	0.10-0.25	1.50-2.50	–
DP-3W	S39274		0.03	24.0-26.0	6.8-8.0	2.5-3.5	1.0	0.24-0.32	0.20-0.80	1.50-2.50
2507	S32750	1.4410	0.03	24.0-26.0	6.0-8.0	3.0-5.0	1.2	0.24-0.32	0.50	–
Zeron100	S32760	1.4501	0.03	24.0-26.0	6.0-8.0	3.0-4.0	1.0	0.20-0.30	0.50-1.00	0.50-1.00

Tab. 1 Chemical composition of modern wrought DSS compared to first generation DSS [6]

The chemical composition we can see in tab. 1 includes also the first generation of duplex stainless steels as a reference point.

Another way to classify DSS is to define the corrosion resistance of duplex grades by their PREN number [5] as defined by:

$$PREN = \%Cr + 3.3\%Mo + 16\%N$$

PREN is a measurement of the corrosion resistance of various types of stainless steel, and does not provide an absolute value for corrosion resistance and cannot be applied in all environments. In some DSS the addition of W can increase corrosion resistance. For these alloys, the pitting resistance is expressed as PREW, according to:

$$PREW = \%Cr+3.3\%Mo+1.65\%W+16\%N$$

The PREN or PREW number is commonly used to classify the family to which an alloy belongs.

Family	UNS	C	Cr	Ni	Mo	W	Cu	N	$PRE_{N/W}$
Lean Duplex	S32101	0.03	21.5	1.5	0.3	-	-	0.22	25
	S32304	0.02	23	4	0.3	-	0.3	0.10	25
Standard Duplex	S31803	0.02	22	5.5	3.	-	-	0.17	35
	S32205		22.5	5.8	3.2	-	-	0.17	36
Superduplex	S32750	0.02	25	7	4.0	-	0.5	0.27	43
	S32760	0.03	25	7	3.5	0.6	0.5	0.25	42
Superaustenitic									
904L	N08904	0.02	20	24.5	4.2	-	1.5	0.05	35
254 SMO	S31254	0.02	20	18	6.1	-	0.7	0.20	43
Austenitic									
304L	S30400	0.02	18.2	8.1	0.3	-	-	0.07	20
316L	S21600	0.02	16.3	10.1	2.1	-	-	0.07	24
317L	S31703	0.02	18.4	12.4	3.2	-	-	0.07	30

Tab. 2. Chemical composition and PRE number of the most common DSS and austenitic stainless steels

A summary, in Tab. 2, shows some examples of different stainless steels grades, i.e. duplex, austenitic and superaustenitic grades with their main alloying components and the PREN/W

number. The superduplex grades with a pitting index PREN/W >40, contain 25% Cr, 6.8% Ni, 3.7% Mo and 0.27% N, with or without Cu and/or W additions (SAF 2507, UR52N, DP3W, Zeron100).

1.4 MICROSTRUCTURE AND COMPOSITION

The behaviour of a duplex stainless steel is due to an optimized microstructure that is characterized by the presence of two phases, austenite and ferrite, in a suitably balanced ratio.

Each of the two phases performs specific tasks: the ferrite provides the mechanical strength and the resistance to stress corrosion cracking, while the austenite ensures a certain ductility, so that together with the 50/50 constitute a microstructure which enjoys high mechanical characteristics and good resistance to corrosion.

To obtain the optimal characteristics of such steels and for their correct use it is important, if not essential, to know in depth the physical metallurgy, the kinetics of precipitation of undesirable phases and the variables that happen on them. The biphasic structure of this family of steel on one hand determines the commercial success but, at the same time, brings with it certain intrinsic hazardous characteristics; the duplex are affected by the precipitation of harmful secondary phases that lead to a net decrease in toughness and / or corrosion resistance. It is therefore of fundamental importance to define the parameters that affect and influence these transformations in order to avoid the formation of brittleness' phase during the production cycle or otherwise harmful phases which could irreparably compromise the properties of the duplex.

The biphasic microstructure is due to the presence in the chemical composition of these steels of an appropriate proportioning of *alfa-stabilizer* and *gamma-stabilizer* elements. Ferrite-stabilizers (Chromium, Molybdenum, Titanium, Vanadium, Tungsten, Silicon, ...) extend the ferrite stability range of α and δ; Austenite-stabilizer (Nickel, Carbon, Manganese, Nitrogen, ...) extend the austenite stability field. These elements are not divided evenly between the two phases.

The ferrite-stabilizers are concentrated in the ferrite, while the austenite is enriched in austenite-stabilizers according partition coefficients that depend on the solubilisation temperature and the chemical composition of the steel. State

diagrams are an essential reference for setting both the working conditions such as treatment condition to obtain the optimal structure and the use limit condition.

Unfortunately the composition of the duplex includes 6 or 7 important elements and is too complex to be described with the usual state diagrams. Therefore we have to use simplified diagrams as the pseudo-binary diagrams or sections of the ternary Fe-Cr-Ni diagram.

Schaeffler introduced the concept of Ni and Cr equivalent predicting phase equilibrium and fields existence of the structures obtained according to the chemical composition of the alloy. This means that these alloys promote the formation of ferrite or austenite, so if the ferrite-stabilizer ability is related to chromium and the austenite-stabilizer is related to nickel it is possible to measure the total amount of ferrite and austenite stabilizing the effect of this elements into the steel.

Thanks to the industrial acquired experience, these diagrams were modified to take account of the different metallurgical states: forged metal, laminate, welding with or without heat treatment etc.

The values of Ni and Cr equivalent can be calculated using the formula:

$$Ni_{eq}=\%Ni+35*\%C+20*\%N+0,5*\%Mn+0,25*\%Cu$$

$$Cr_{eq}=\%Cr+\%Mo+1,5*\%Si+0,7*\%Nb$$

The Fig. 3 is used for the previous concept of Nieq e Creq and show the ferrite levels in bands, both as percentages, based on metallographic determinations. [4][9][10]

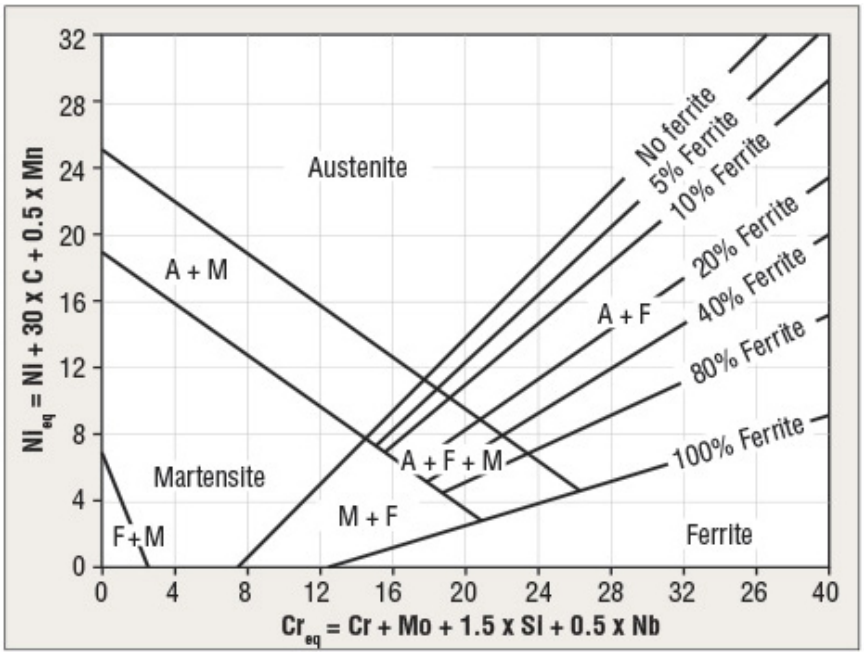

Fig. 3: Schaeffler-Delong diagram with showed the ferrite level in bands as percentage

The *pseudo-phase* diagrams of DSS are much easier than the ternary. These charts provide important information on the duplex microstructures and their evolution, as the temperature changes. Fig. 4 shows that after a primary solidification in the ferritic phase, the microstructure is partly transformed into austenitic phase during the subsequent cooling at room temperature.

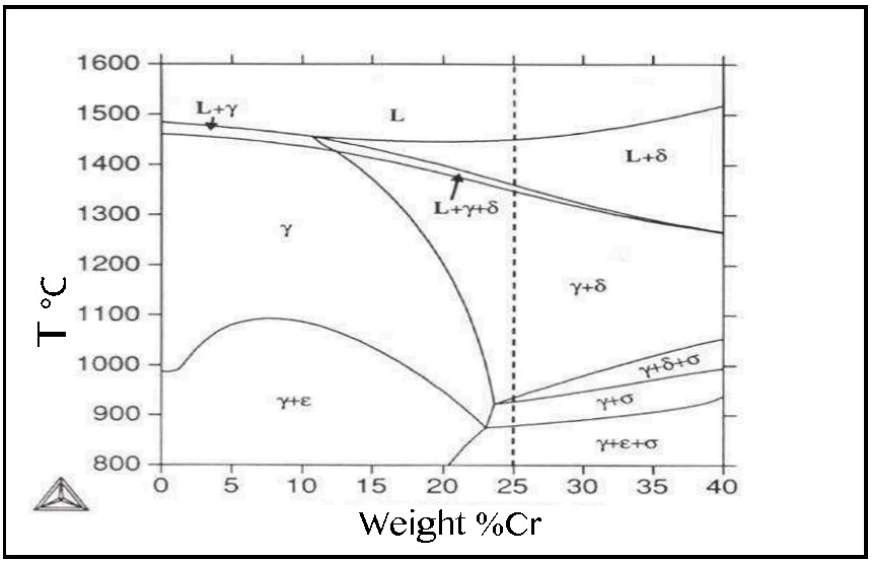

Fig. 4: State diagram at above 800 ° C. The dotted line refers to the composition of the super duplex 2507.

1.5 PHASE TRANSFORMATION

Between 300°C and 1100°C duplex stainless steels can present the precipitation of secondary phases or intermetallic phases that modify their properties. The "standard" duplex phases (γ and δ) in this temperature range, can lose their stability, with consequent risk of precipitation due to the fact that some alloy elements, in particular chromium and molybdenum, tend to migrate from the solid solution of the matrix to form intermetallic compounds, whose kinetics of precipitation are most often very slow.

Most of the elements in the alloy tends to broaden the temperature range whose intermetallic precipitation are likely to increase the rate of formation as shown in Fig 5. which shows the TTT diagrams for the main types of duplex stainless steels; it is clear that there are two critical intervals of temperatures in which there is the formation of secondary phases.

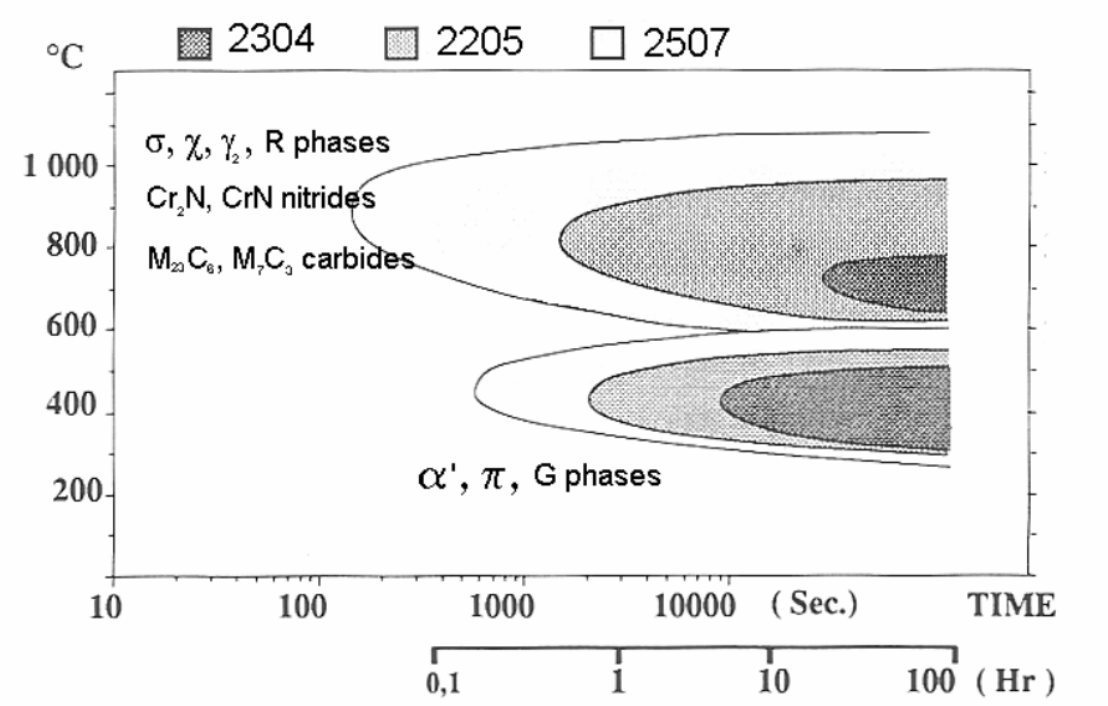

Fig 5: TTT diagram for the most used duplex stainless steel

Taking a look again at fig 4 we can see how the austenite, sigma and Cr_2N are consider, for 2507 grade, thermodynamically stable at 800°C.

Anyway, between the range temperature 300-1100°C many secondary phase can precipitate on the DSS. It possible to identify two main intervals where the precipitation is stronger.

The first is the *"475°C Transformation"* where the spinodal decomposition occurs, which is a demixion of the ferrite in high and poor Cr contents. It's possible to notice a subsequent hardening and embrittlement. DSS are sensitive to this phenomena, that is the reason why most of applications are strictly restricted to a temperature lower than 250-280°C.

The second interval is between 650-900°C in which the ferrite phase is thermodynamically unstable. In this range occurs the eutectic decomposition of the ferrite that decompose into σ-phase and γ'-phase. It has also been observed a partially precipitation of χ-phase. It is well known that σ-phase precipitate in all the duplex stainless steel, but this is even more emphasized in the SDSS due to the high amount of Mo and Cr which move the formation curves of σ-phase and other phase towards left.

It's a matter of fact that Mo increase the stability range of the σ-phase to higher temperature. The σ-phase is brittle and affect the ductility at elevated room temperature: a small amount of σ-phase reduce heavily the toughness of the steel even though the tensile properties are not affected to the same extent.

As already seen in Fig 4. the dotted line indicate the DSS 2507 grade, and following the line we can observe that there is a wide temperature range (950-1300°C) in which ferrite and austenite are stable together. After 800°C we find only σ-phase, Cr2N *"ε"*, and austenite as stable phase.

It is important to notice that the corrosion resistance is a very important characteristic of this kind of steel, although after the eutectic decomposition of ferrite we observe a relevant decrease of the corrosion resistance: The presence of σ-phase decreases resistance to localized corrosion, due to the depletion of chromium in the surrounding areas of the precipitates σ-phase.

It’s already known that if we make a plastic deformation in steel the amount of internal energy increases, which depends on the rate of deformation. Moreover after a plastic deformation the tensile strength increases too.

It is quite difficult the analysis for DSS, because their composition is given by two different phases, one is the ferrite phase (BCC) and the other is the austenite phase (FCC). The first one is more resistant, has few slip planes and needs a higher critical stress to activate the first slip plane. In the case of austenite, it is required a lower activation stress and therefore is easier to deform.

As written above, σ is a non-magnetic phase with a tetragonal structure. It normally starts growing at the ferrite boundary and keeps growing into the grains in a cellular structure form (Fig 6). After that it grows into austenite grains but slower than into the ferrite grains because the diffusion rate is higher on the δ-phase.

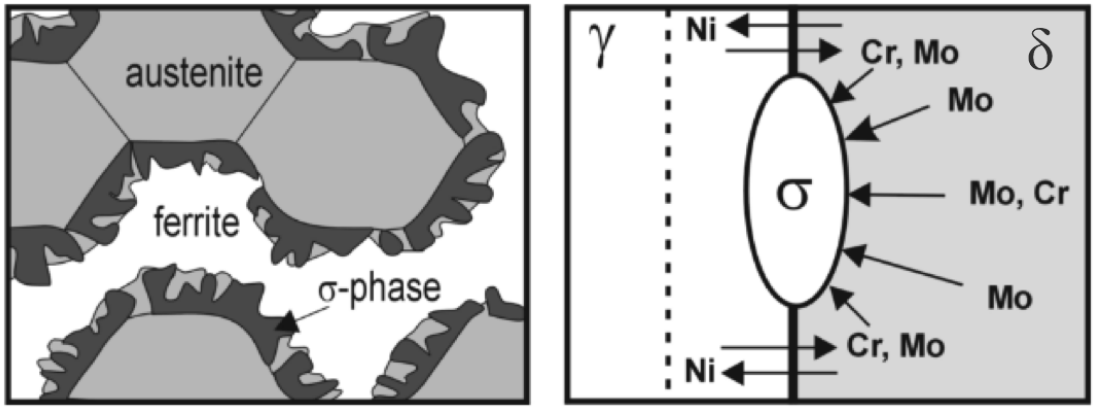

Fig 6: Diagram of σ-phase nucleation at ferrite/austenite grain boundaries.

There are many articles which have analysed the behaviour of the eutectic composition in duplex stainless steel, and it has been noticed that previous cold rolling deformation causes an increase of the rate of ferrite decomposition:

$$\delta \rightarrow \sigma + \gamma'$$

Previous works have been centred on investigating the effect of plastic deformation on the precipitation of sigma phase: it has been found that in

austenitic steel cold rolled at 20% deformation, cell structure and twins crossing are kept stable also for temperature of 550°C. [11][12][13]

1.6 APPLICATIONS

Applications of duplex stainless steels are usually those requiring high strength and excellent corrosion resistance. The typical sectors are mainly oil production, petrochemicals and desalination plants. DSS are used in oil production industry thanks to their resistance in conditions of SCC and localized corrosion [7]. For this reason DSS are frequently used in oil-refinery heat exchangers where the exposition to chloride-containing process streams, cooling waters or deposits is consistent.

Fig. 7 Standard duplex 2205 Heat Exchanger pipe

Superduplex S32750 are suitable in piping and process equipment for oil/gas industry. Usually when the corrosive conditions are severe and complex, due to high chloride concentrations and overheating. Therefore more alloyed DSS are required to prevent the risk of premature failure.

In presence of organic acids, which can cause corrosion problems, duplex and super duplex, such as S32803 / S32205 and S32750 were found to be suitable materials for that kind of applications.

Duplex stainless steels are also used in desalination plants[8], but due to the high costs of alloying elements, like Ni and Mo, that is not the most effective solution.

Recent statistic data shows that traditional applications as oil and gas, offshore and petrochemical declines from 27% to 7%.

There is a relative decline also in chemical, storage and transportation, while we can see increased market share include (waste) water (9% to 18%), construction and civil engineering (6% to 12%), power generation (1% to 7%) and other applications[1].

CHAPTER 2

EXPERIMENTAL PROCEDURE

The analysed material is the UNS S32750 (SAF2507) Duplex Stainless Steel the composition has been reported in the table below (Tab 3):

Meteriale	C	Si	Mn	P	S	Cr	Ni	Mo	Cu	N
2507	0.015	0.24	0.83	0.023	0.001	24.80	6.89	3.83	0.23	0.27

Tab 3. Chemical composition of DSS 2507

2.1 SAMPLE PREPARATION

At the beginning the original bar has been supplied by Outokumpu and was hot rolled and annealed. This bar has been cut into 35 pieces with this dimensions:

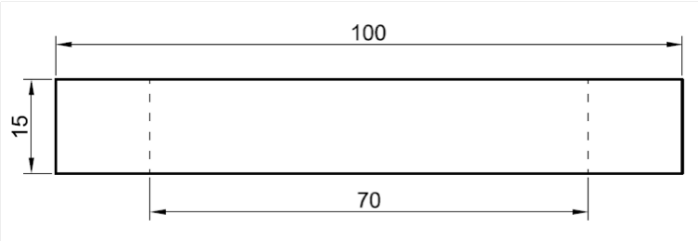

Fig 9. Samples dimensions in mm

Fig 10. Samples after different cold rolled deformation

Once samples were prepared, we cold rolled them in perpendicular direction to the original grain orientation (to avoid continuous casting weak).

The thickness reduction were: 10% - 20% - 30% - 40% - 50% - 60%

5 out of 35 samples were not cold rolled to be used to compare with the other deformation samples.

After cold rolling the samples had been heat treated at different temperatures: 700°C – 750°C – 800°C – 850°C for 30 minutes.

Due to the big amount of specimens, the table below (Tab 4) explain much better the situation.

	Cold rolled deformation (%)						
Heat Treatment Temperature (°C)	0%	10%	20%	30%	40%	50%	60%
20	1	6	11	16	21	26	31
700	2	7	12	17	22	27	32
750	3	8	13	18	23	28	33
800	4	9	14	19	24	29	34
850	5	10	15	20	25	30	35

Tab 4. Specimens table with heat treatment and cold rolled deformation

Once all the samples were heat treated, they were cut into squares 15mm-side and, to make the handling easier, they were put into a epoxy resin (Fig 11). Then all the samples has been first grinded with SiC papers starting from P60 up to P2400 and after that for polishing we used clothes with diamond suspension at 3µ and 1µ.

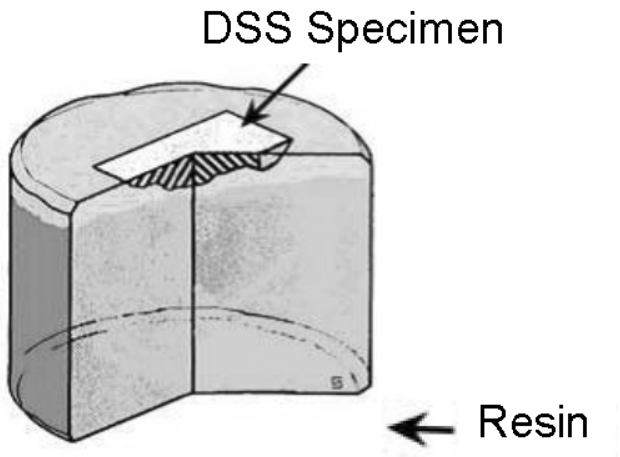

Fig 11. Specimen embedded in resin

Fig 12. Final result after grinding and polishing

2.2 OPTICAL MICROSCOPY ANALYSIS

The optical microscope was used for the micrographic observation of the samples. OM technique is usually the first step for metallic materials analysis and crucial importance is the search for presence of possible precipitating compounds on the grain boundaries. Moreover this technique can help in cracks' search, porosity and injuries especially in the samples that has been heavily cold rolled, and we have seen the dimensional and directional change of ferrite and austenite grains.

OM technique has two main limits:

- Poor resolving power, less than 0.2 microns.
- Inability to focus on details placed on different levels (field's depth).

The analysis was performed by Olympus PMG 3 with different magnification (25x – 50x – 100x – 500x – 1000x) on the two cold rolled directions (longitudinal and transversal). Photos have been taken for each magnification and each direction.

After polishing the specimen surface, observed under the microscope, is specular and it's impossible to evaluate it. For this reason we have to do a chemical attack on the specimen surface in order to allow, through a selective action, differentiation of the various crystalline alloy components and phases. This chemical attack is called *etching*. Once the sample was put into the chemical reagent for less than 20sec, its components will be attacked according to their reaction rate: the result is the formation of different levels and different coloration for each component. In other words the surface is no longer specular but shows the different phases in different colours. The chemical reagent chosen for the duplex steel 2507 is the Beraha, which the composition is given in Tab 5.

Reagent	Chemical composition
Beraha	- 100ml H_2O - 20ml HCl - 1g $K_2S_2O_5$

Tab 5. Etching composition of Beraha

This chemical attack makes the ferrite phase darker and austenite phase white. [4][9]

During the analysis of the results you have to consider the measurement error. If you want to give an analytical expression to error bands in the measurements taken, you can be assessed by standard deviation, denoted by s and defined by the equation:

$$s = \sqrt{\frac{\sum_{i=1}^{n}(xi - x_A)^2}{n-1}}$$

where:

- n is the numbers of measurements done
- *xi* is analysis value
- x_A is the average of the values taken defined as

$$x_A = \frac{\sum_{i=1}^{n}(xi)}{n}$$

2.3 ELECTRON BACKSCATTER DIFFRACTION (EBSD)

Electron Backscatter Diffraction (EBSD) is a microstructural-crystallographic characterisation technique to study any crystalline or polycrystalline material. The technique allows us to understanding the structure, crystal orientation and phase of materials analysed.

EBSD is conducted using a SEM equipped with an EBSD detector. Scanning Electron Microscope (SEM) is a type of electron microscope that produces images of a specimen by scanning it with an electron beam. The electrons from the beam interact with atoms in the sample, producing various signals that give us information about the sample's surface and composition.

The sample is placed in the SEM and inclined approximately 70^{o} relative to normal incidence of the electron beam. The detector is a camera equipped with a phosphor screen (Fig 13). Once the electron beam strikes the sample the diffracted electrons form a pattern on the phosphor screen which is fluoresced by electron from the sample to form the diffraction patter.

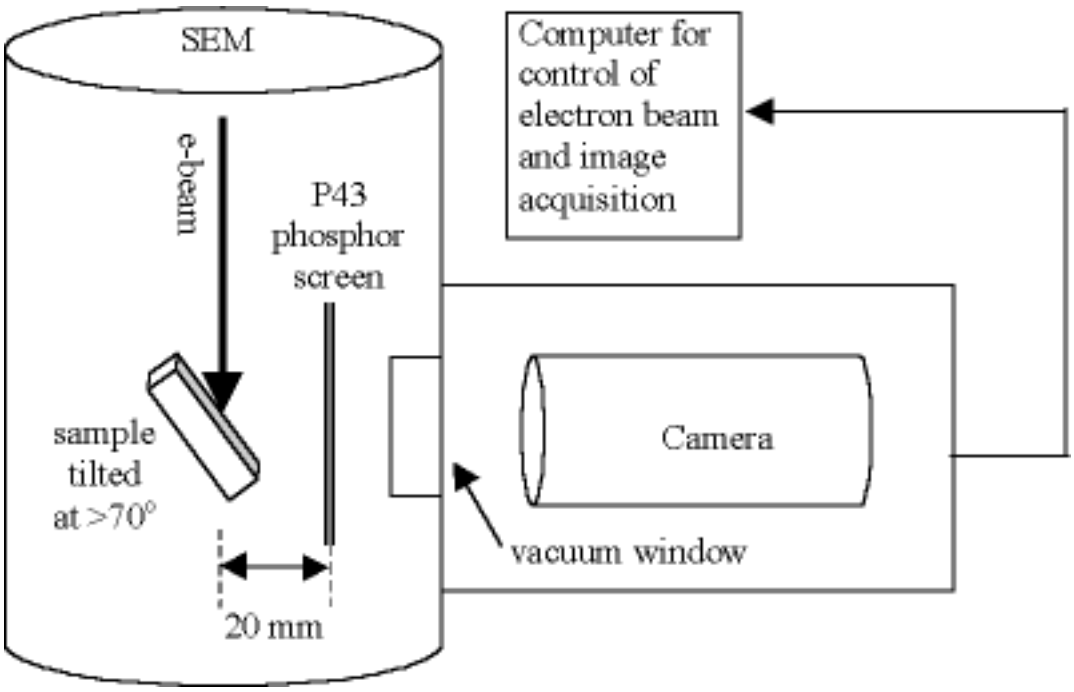

Fig 13. Scheme of the EBSD technique

The phosphor screen is located within the sample chamber of the SEM at an angle of approximately 90° to the pole piece and is coupled to a compact lens which focuses the image from the phosphor screen onto the camera. In this configuration, which electrons which enter the sample backscatter and may escape. Leaving the sample, electrons may exit at the Bragg condition related to the crystalline structure and diffract.

These diffracted electrons can escape the material and some will collide and excite the phosphor screen make it fluorescent.

The specimen is put under high vacuum (10^{-5} Torr) and has to be conductive otherwise it produces electrostatic charges which disturb the detection of the electrons. EBSD allows to analyse the sample at the polished state, without chemical etching, since the image contrast derives from the different chemical composition of the phases. In addition the chemical attack, may lead to difficulties of distinctions of the phases, like precipitates species of small size. Another advantages of electron microscopy is the chemical analysis of the microstructural phases.

The image analysis for the determination of the volume fractions of secondary phases χ and σ is a delicate operation and it depends on the ability of the operator.

The image analysis stages, after acquisition by SEM, involving the processing of the image in terms of contrast, illumination and balance to make the difference between the microstructural phases possible. It follows the step of segmentation that involves the selection of the grey level of the microstructural phase to quantify; This is possible thanks to the binarization of the grey scale for the pixels of the image.

2.4 HARDNESS TEST

Hardness is a measure of resistance that quantifies how resistant a solid material is when a compressive force is applied on it.

For my study has been used KB Prüftechnik with a 200g load. The time load applied is in a range between 10 and 15 seconds.

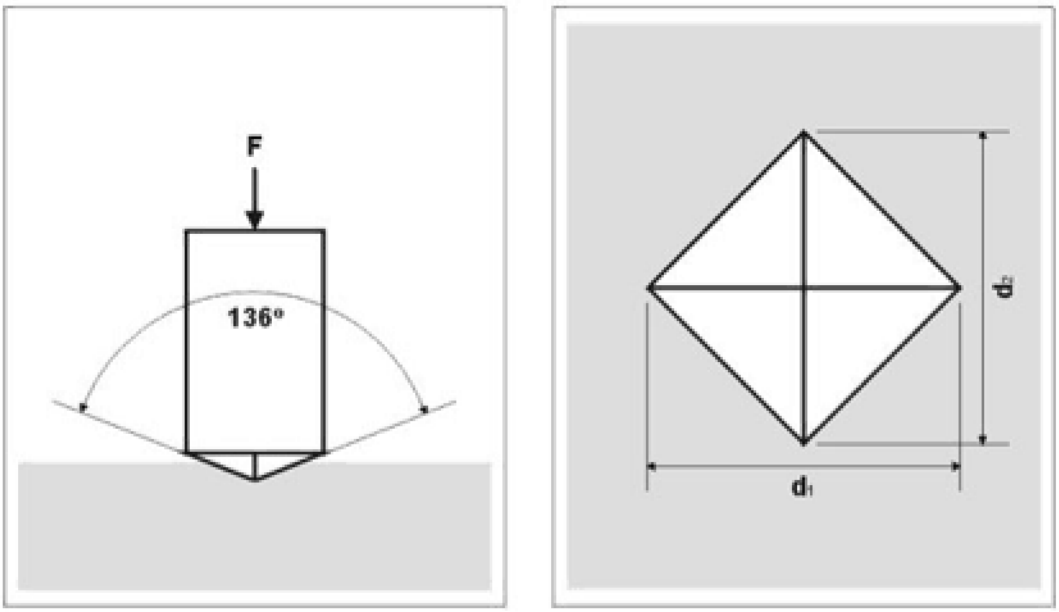

Fig. 14 Indentation shape

The test consists of measuring the diagonal *d* of the indentation shape made by a diamond indenter with a square base. (Fig. 14)

Knowing the applied load (g), we can obtain the value of the Vickers hardness following the equation:

$$HV = 1.854 \frac{P}{D} \left[\frac{Kg}{mm^2}\right]$$

Where P is the load in kg and D is the average length of the diagonal left by the indenter in millimeters.

2.5 X-RAY DIFFRACTION

XRD test has been performed in the University of Miskolc with a Stresstech Xstress 3000 G3 (Fig 15) which is an accurate and portable X-ray diffractometer for measuring residual stresses and retained austenite contents. The machine measures the stresses on crystalline material by Xrays, based on the phenomenon known as Bragg´s law:

$$n\lambda=2d\sin(\theta)$$

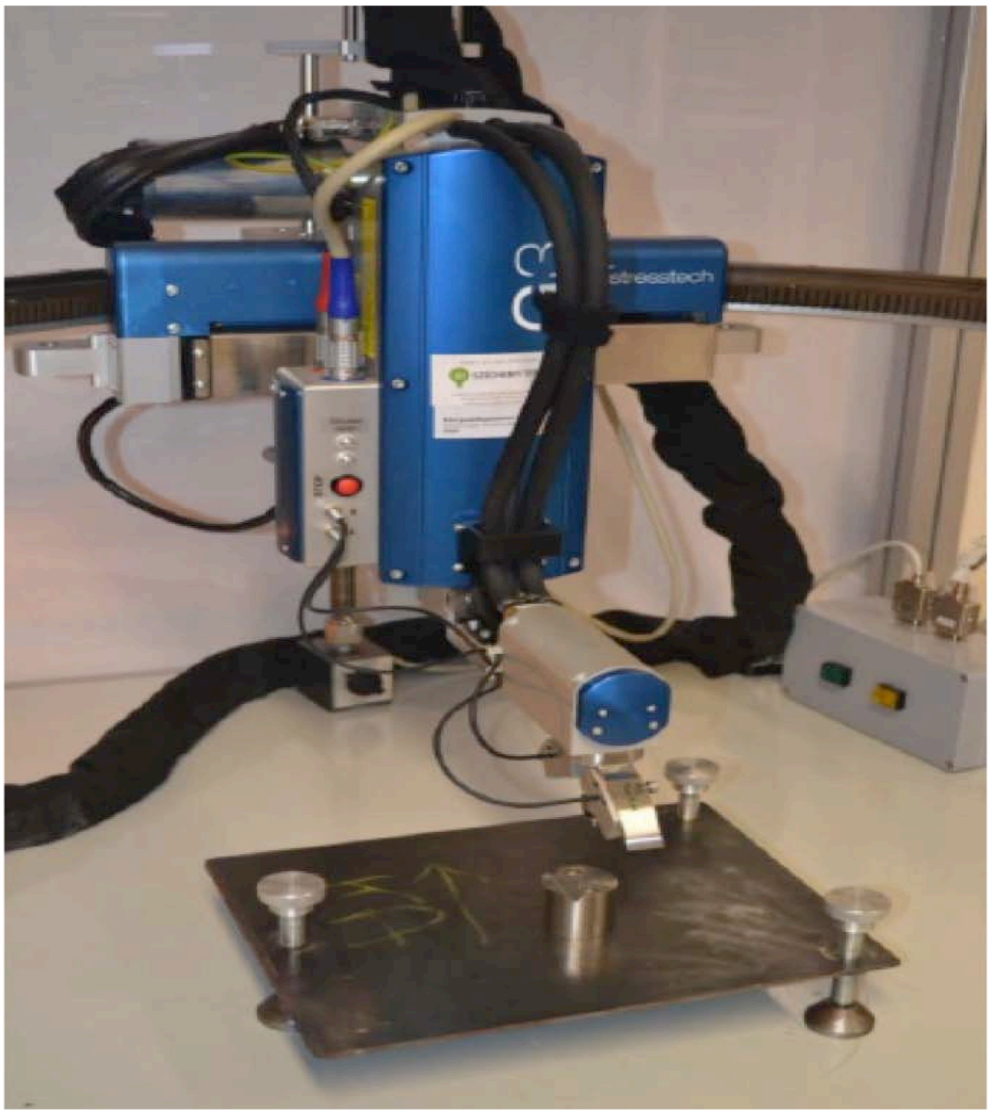

Fig 15. Xstress 3000 G3 / G3R – Portable X-ray Diffraction (XRD)

Where λ is the wavelength of the radiation, d is the distance between two planes and θ is the scattering angle.

According to the lecture, the crystal lattice is made by atoms that are set together to form a sequence of parallel planes that divide each other by a distance *d*, which depends on the nature of the element.

For a better comprehension on how XRD work follow the Fig 16.

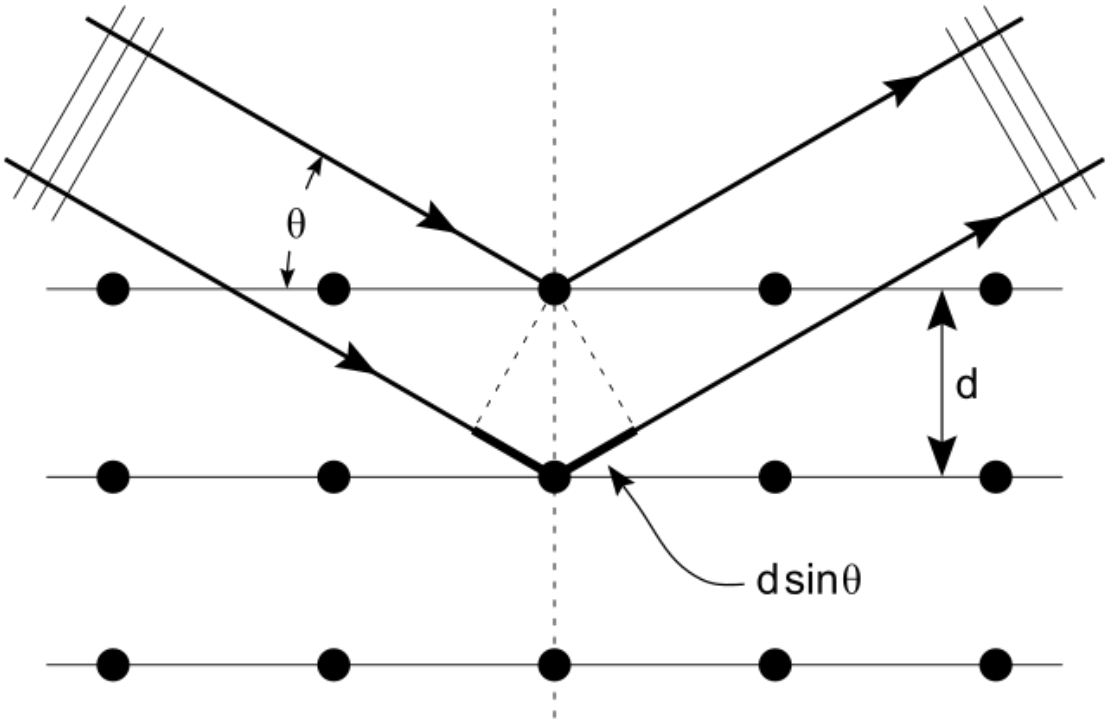

Fig. 16 How the X-Ray can be reflected by the crystal planes[29]

The incoming beam (coming from left) causes each scattered atoms to re-radiate a small portion of its intensity as a spherical wave. If scattered atoms are arranged symmetrically with a separation d, these spherical waves will be synchronized only in directions where their path-length difference 2dsin(θ) equals an integer multiple of the wavelength λ. In that case, part of the incoming beam is deflected by an angle 2θ, producing a reflection spot in the diffraction pattern.[14]

The base of the quantitative phase analysis is that $I_{x,hkl}$ intensity of whichever X-ray diffraction reflection of a phase is proportional with Vx, where Vx is the volume of the phase. The formula has been reported here:

$$I_{x,\,hdl} = C * W * (HT) * |F|^2 * N^2 * A * D * V_x = G * A * V_x$$

where

C is the equipment factor

W is the angle factor and is defined as

$$W = \frac{1 + \cos^2 2\theta}{cos\theta * \sin^2 \theta}$$

where θ is the Bragg angle.

HT is the surface probability. In case of isotropic polycrystalline material (T = 1), this area is proportional with H. The H factor expressing how many equivalent (hkl) planes has the given crystal. Tab 6 has been used to define the hkl planes:

Miller index	H
{h00}	6
{hh0}	12
{hhh}	8
{hk0}	24
{hkk}	24
{hkl}	48

Tab 6. Relation between Miller index and H factor

N is the unit cell number per unit volume defined as

$$N = \frac{1}{a^3}$$

where a is the lattice parameter.

A is the absorption factor defined as

$$A = \frac{1}{2\mu}$$

where μ is the average mass absorption coefficient, which depends on the volume ratio of the phases present, that is, what we are looking for.

F^2 is a structural factors and has defined as

$$F_{(hkl)}^2 = [f_1 \cos\{2\pi (hi_{11} + ki_{12} + li_{13})\} + f_2 \cos\{2\pi (hi_{21} + ki_{22} + li_{23})\} + \ldots + f_n \cos\{2\pi (hi_{n1} + ki_{n2} + li_{n3})\}]^2 + [f_1 \sin\{2\pi (hi_{11} + ki_{12} + li_{13})\} + + f_2 \sin\{2\pi (hi_{21} + ki_{22} + li_{23})\} + \ldots + f_n \sin\{2\pi (hi_{n1} + ki_{n2} + li_{n3})\}]^2$$

D is the temperature factor (Debye-Waller factor).[18]

2.6 MAGNETIC TESTS

Regarding duplex stainless steel, magnetic tests are a valid instrument for analysis. They can be used to find any kind of variation of ferromagnetic phase content in the material.

In ferromagnetic materials there isn't a linear correlation between B and H. First of all, for equal current, the magnetic field that is produced in them is much more intense (up to 10 000 times greater). Also a phenomenon called magnetization saturation occurs whereby the magnetic field no longer increases once it has reached a certain value for each material. No matter how much current flows into the solenoid: beyond a certain limit $\vec{B}$ stops growing.

The situation is represented by the following figure (Fig 17)

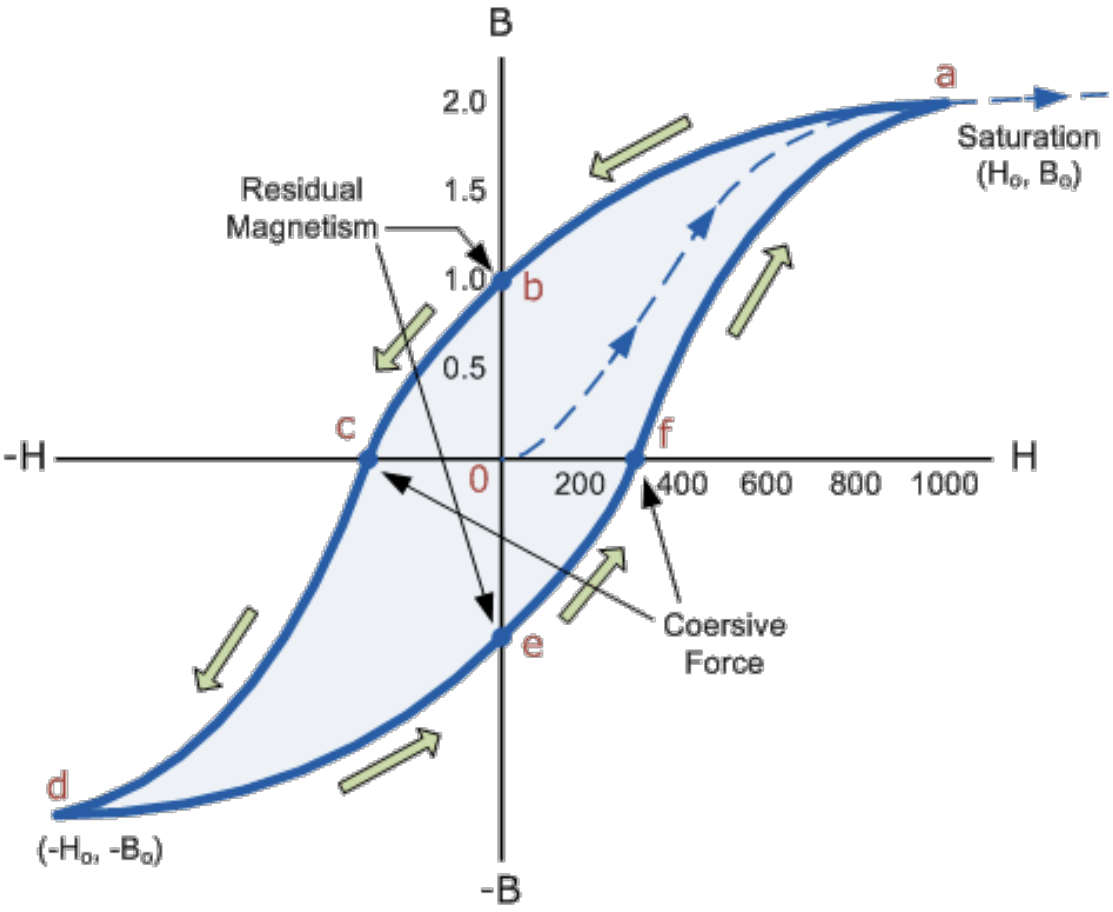

Fig 17. Diagram of magnetic hysteresis loop

The hysteresis curve (Fig 17) shows the behaviour of a ferromagnetic material: it starts at point 0 of the magnetization curve in which the value of B and H is zero and the material is demagnetised.

If we increase the magnetisation current, I, in a positive direction to some value the magnetic field strength H increase as well as the flux density B also increase as shown by the (Fig 17) from *0* to *a*.

The point b in the hysteresis curve is due to the residual magnetism present in the material. To lower the flux density at point b to 0 we need to reverse the current flowing through the coil. The magnetising force which must be applied to null the residual flux density is called a "Coercive Force". This coercive force reverses the magnetic field, re-arranging the molecular magnets until the core becomes demagnetised at point c.[17]

In this work I have conducted the following magnetic test: Stäblein-Steinitz test, Eddy-Current test and Fischer-Ferrite test.

2.6.1 STÄBLEIN-STEINITZ TEST

Stäblein-Steinitz tester is a direct current close circuit conceived to reach high coercivity and magnetization field with specimens that have small dimensions ratio. It's based on two iron yokes placed faced each other with an air gap between the opposite surface (Fig 18)

In both yokes, two excitation coils are placed at the end of each "arm". There is a connection between the two yokes so their magnetic fluxes circulate in the same direction inside the yokes circuit.[26]

If a sample was placed into the measuring air gap it upsets the symmetry of the yoke and there will be a magnetic flux thought the bridge-branch. The flux of the bridge-branch can be calculated by a simple concentrated parameter model of the magnetic circuit. After the proper simplifications it can be derived.

$$\mu_0 M_{sample} = B_{Bridge} \frac{C_1(1 + \frac{C_2}{l})}{A}$$

This demonstrates that the magnetic polarization of the measured sample is linearly proportional with the magnetic induction detected within the bridge-branch. [15]

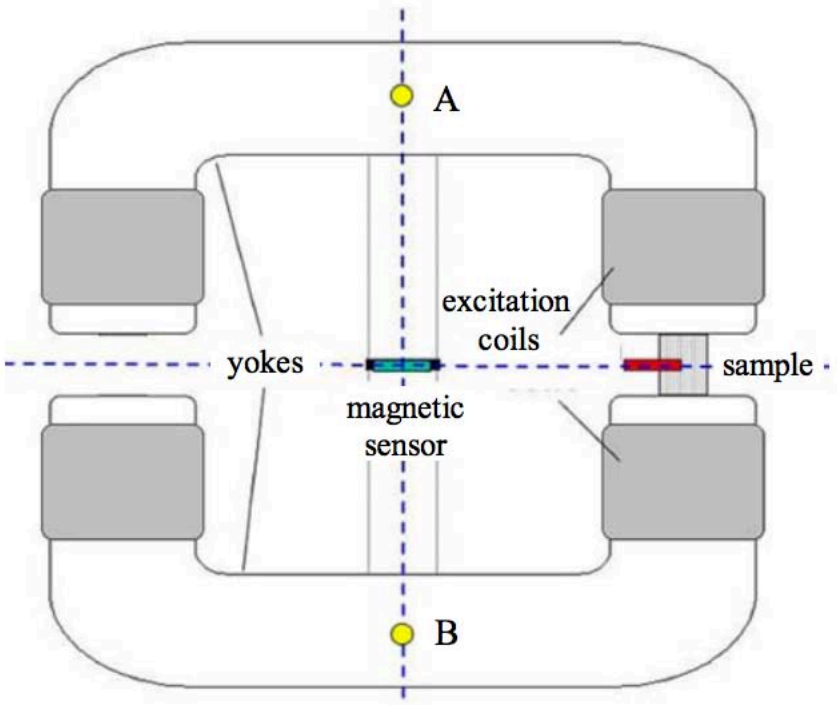

Fig 18: The schematic of the Stäblein-Steinitz set up [15]

For the Stäblein-Steinitz type magnet tester, the calibration is one of the most important parameters for our measurements because an incorrect calibration would render the data collected, useless.

If the system runs without any specimens the results should be a horizontal line, otherwise a calibration is required.

Stäblein-Steinitz measurements are specific for testing bulk material, and we are not in that condition. In our case the specimens have been cut into 4 square pieces of side 15mm, with the purpose of creating a block sample for each specimen.

We have also calculated the cross section of each block to compare it with the reference block: the calibration show a proportional relation between the cross section of the sample and the saturation magnetization value, and thank to the Stäblein-Steinitz software, knowing the exact specifications of the aluminum block, took as reference, we can obtain directly the real magnetization value of the specimens. [4][16][21]

2.6.2 EDDY-CURRENT TEST

Eddy current testing is based on the physics phenomenon of electromagnetic induction. For a better comprehension look at the Fig 19.

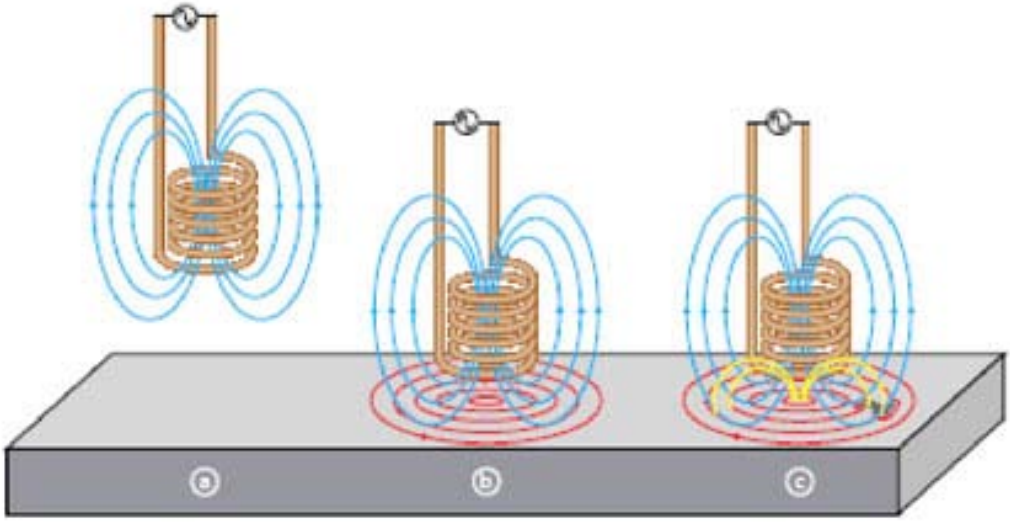

Fig 19. Eddy-Current tester explanation[33]

In an eddy current probe, an alternating current flows through a wire coil at a chosen frequency and generates an oscillating magnetic field around the coil *(a)*. When the coil is placed close to an electrically conductive material, like our duplex steel sample, a circular flow of electrons known as *eddy current* will start to move through the metal; in other words eddy current is induced in the metal *(b)*. That eddy current flowing through the metal will in turn generate

its own magnetic field, which will interact with the coil and its field through mutual inductance. Changes in the sample composition or defects like near-surface cracking will interrupt or modify the amplitude and pattern of the eddy current and the resulting magnetic field. This affects the movement of electrons in the coil by varying the electrical impedance of the coil. With a software is possible to plots changes in the impedance amplitude and phase angle, which can be used to identify changes in the test sample.[30]

In this work Eddy-Current test has been done at four different frequency: 10.0KHz – 40.0KHz – 66.7KHz – 100.0KHz

2.6.3 FISCHER-FERRITE TEST

For this work has been used the FERITSCOPE FMP30 by Fischer®, which is an instrument for measuring the ferrite content in austenitic and duplex steel according to the magnetic induction method.

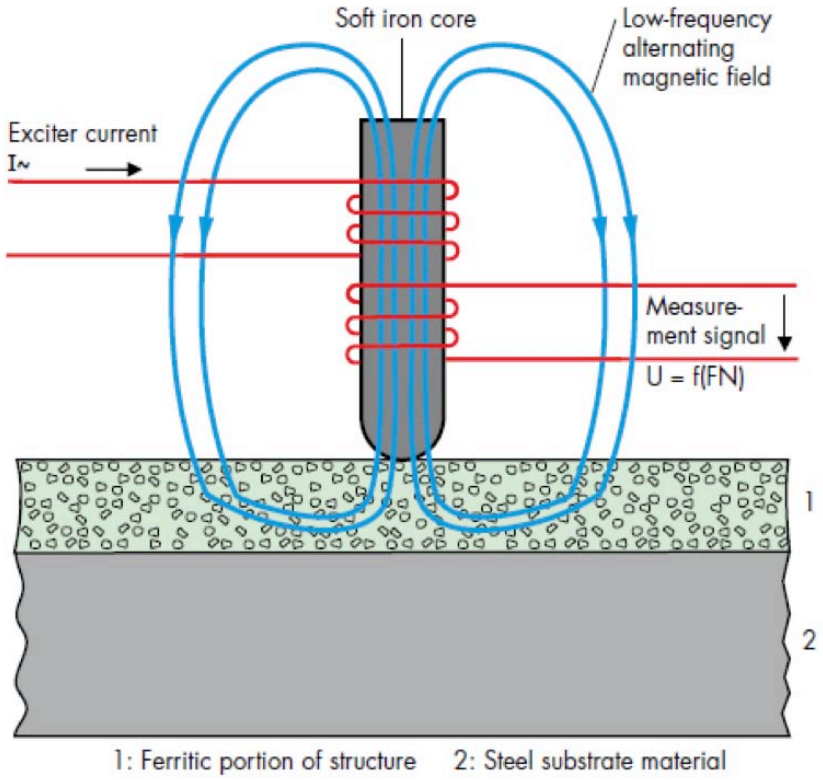

Fig 20. Fischer-Ferrite tester explanation

The Fischer-Ferrite tester principle is quite simple: a magnetic field generated by a coil is put in contact with the magnetic component of the specimen. The variations in the magnetic field lead to a voltage, which is proportional to the content amount of ferrite in the second coil. Evaluating the voltage we can obtain the ferrite content.

The FERITSCOPE FMP30 is a portable instrument that can be used to check the ferrite content in loco, It works with a frequency of 1KHz and it's powered by 4x normal R6/LR6 batteries to generate the excitation field required.

This feritscope is an useful instrument for a qualitatively analysis of the ferrite content.[31]

2.7 DENSITY TEST

This test was performed at KFKI Physical Research Institute for particle and nuclear physics in Budapest with the help of the phD P. Zsolt.

We used AccuPyc II 1340 Pycnometer to measure the density the samples. The AccuPyc is a gas displacement pycnometer which measures the volume of solid objects of regular or irregular shape whether powdered or in one piece. A simplified diagram of the instrument is shown in Fig 21.

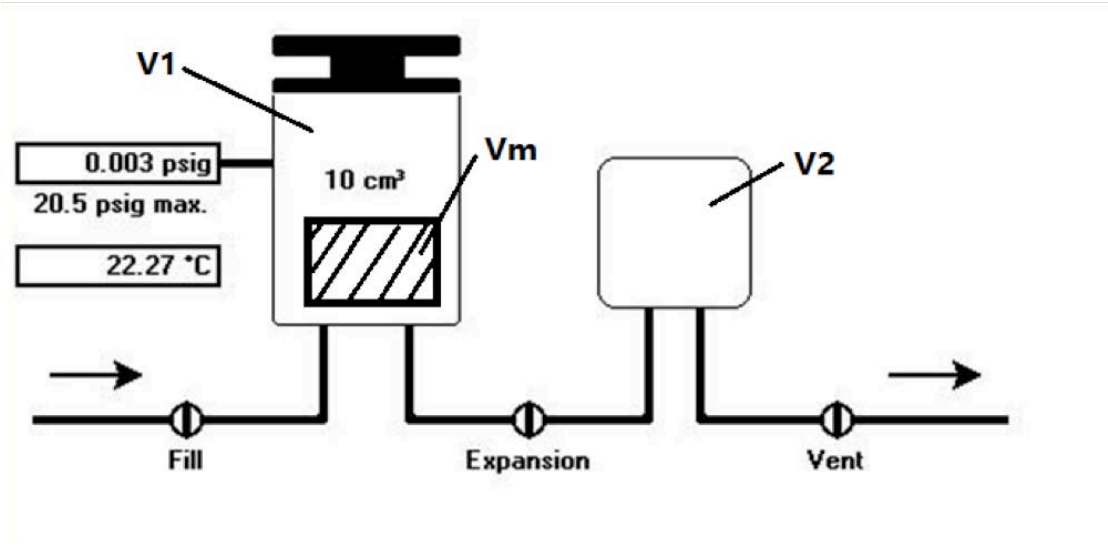

Fig 21. Functional diagram of AccuPyc II 1340 Pycnometer

Assume that both V_1 and V_2 are at ambient pressure P_A, are at ambient temperature T_A and that the three valves are closed. V_1 is then charged to an elevated pressure P_1. The mass balance equation across the sample cell, V_1, is

$$P1(V1 - Vm) = nCRTA$$

where

n_C = the number of moles of gas in the sample cell

R = the gas constant

T_A = the ambient temperature

The mass equation for the expansion volume is

$$PAV2 = nERTA$$

where

P_A = ambient pressure

n_E = the number of moles of gas in the expansion volume

When the valves is opened, the pressure falls to an intermediate value, P2, and the mass balance equation becomes

$$P2(V1 - Vm + V2) = nCRTA + nERTA$$

Substituting from the first two equations into the third:

$$P2(V1 - Vm + V2) = P1(V1 - Vm) + PAV2$$

or

$$(P2 - P1)(V1 - Vm) = (PA - P2)V2$$

then

$$V_1 - V_m = \frac{P_A - P_2}{P_2 - P_1} V_2$$

Dividing by $(P_A - P_2)$ in both the numerator and denominator we obtain

$$Vm = V1 - \frac{V2}{\left(\frac{(P_1 - P_A)}{(P_2 - P_A)}\right) - 1}$$

Since P1, P2 and PA are expressed in equations as absolute pressures and in the last equation is arranged so that PA is subtracted from both P1 and P2 before use, new P1g and P2g may be redefined as gauge pressures

$$P_{1g} = P_1 - P_A$$
$$P_{2g} = P_2 - P_A$$

and we can rewrite the equation as

$$Vm = V1 - \frac{V2}{\left(\frac{P_{1g}}{P_{2g}}\right) - 1}$$

This equation becomes the working equation for the pycnometer. Calibration procedures are provided to determine V1 and V2 and the pressure are measured by a gauge pressure transducer. Provisions are made for conveniently charging and discharging gases at controlled rates, for optimizing the relative sizes of the sample chamber and expansion volumes, and for cleansing the samples of vapours.

The gas used by the Accupyc is He because its structure allows it to enter inside each cavity or porosity of the specimens. [32]

2.8 CORROSION TEST

The last test I performed in Budapest was the corrosion test. It consists in reacting the specimens with a solution of Ferric chloride ($FeCl_3$) for 24, 48 and 72 hours. At the beginning the samples has been cleaned and weighted so that at the end of the test we can compare the results obtained with the initial ones.
The samples were put in particular supports to increase the amount of surface in contact with the iron chloride solution (Fig 22).

Fig 22. Specimens put in supports and ready for corrosion test

There are two different procedures for the determination of pitting and cervice corrosion resistant of stainless steels: 1) Method A: Total immersion ferric chloride test 2) Method B: Ferric chloride cervice test.

The test we performed was the Total immersion ferric chloride test (Method A). Method A is designed to determine the relative pitting resistance of stainless steel.

The Ferric Chloride Test solution is made by dissolving 100g of reagent grade ferric chloride, $FeCl_3{*}6H_2O$, in 900ml of distilled water (about 6% $FeCl_3$ by weight). Then pass through a filter paper to remove the insoluble particles.

Once the solution was ready we started put all the samples in glass container one by one, fill with the solution until the whole specimen was covered and then closed the top.

The specimens were put in the lab for 24, 48 and 72 hours: after each cycle the samples were washed and weighted with a five digit balance.[17]

Fig 23. Samples in ferric chloride solution into glass container

CHAPTER 3

DATA ANALYSIS

3.1 OPTICAL METALLOGRAPHIC ANALYSIS

As explained in chapter 2 all samples have been incorporated into an epoxidic resin and have been investigated both on the longitudinal and transversal side according to the cold rolling direction.

The etchant we used for optical metallographic analysis, Beraha, makes ferrite darker than austenite so we can clearly distinguish between them.

The deformation due to cold rolled has an important effect on the grain's size and shape and this fact can be notice along longitudinal direction as stretching and thinning of austenitic and ferritic grains; different from the transversal direction effects which is a crushing of both grains.

In our analysis, the reduction size of the grains in 40%, 50% and 60% deformation samples is significant that only with 50x or more magnification is possible to distinguish the austenite grains from the ferrite grains.

Therefore the grain's elongation due to the deformation leads to a chopping of austenite, which is emphasized with the increase of the deformation.

We noticed that in the samples 1-6-11-16-21-26-31, which are only deformed without heat treatment, there is no a precipitation of other phases but just a deformation in the grain boundaries due to the cold rolled.

This phenomena has been also seen in a work regarding 2101 lean duplex steel.[4]

The following images show the difference between no deformation and 60% deformation.

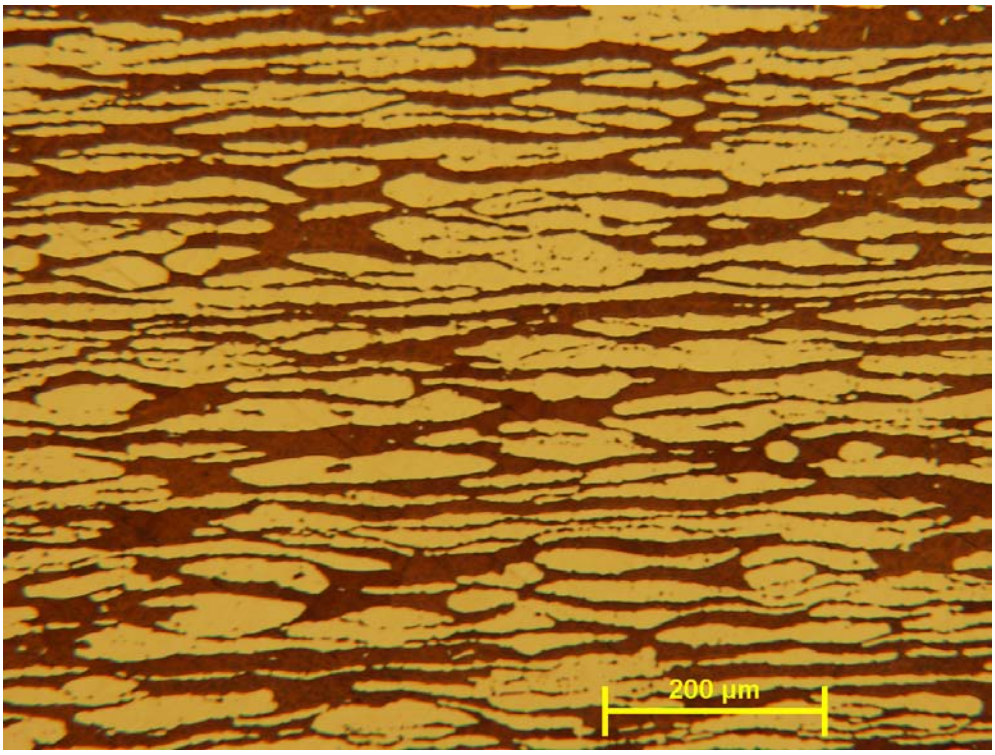

Fig 24. Base Material without heat treatment and deformation 100x magnification

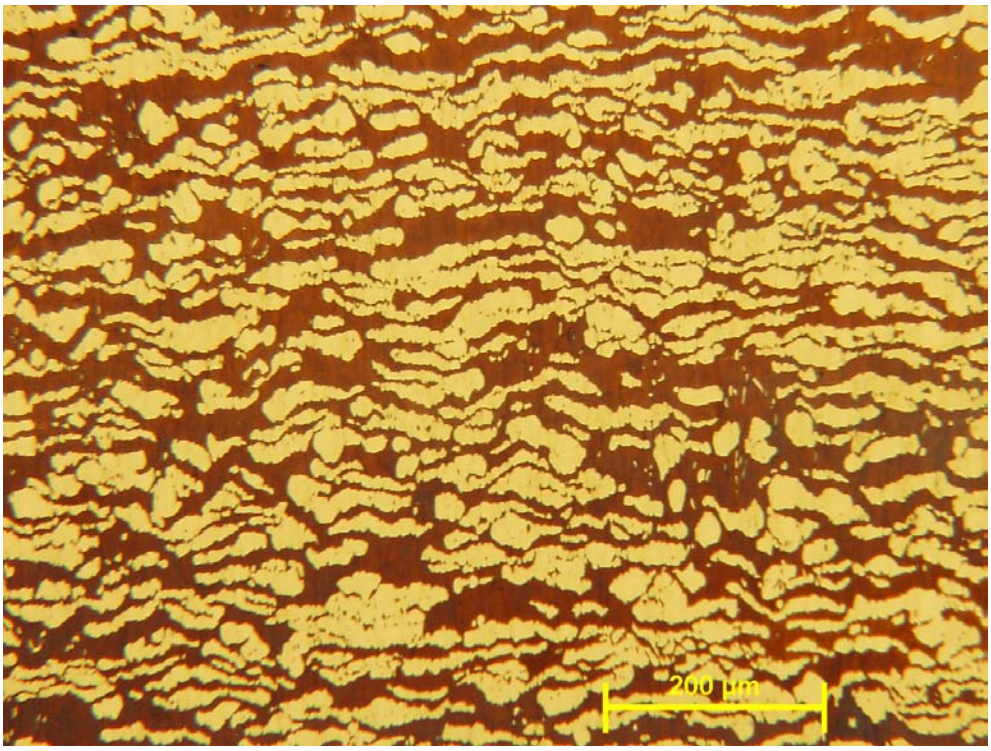

Fig 25. 60% deformation without heat treatment 100x magnification

The main important difference happens on the samples that have been heat treated: at the temperature of 700°C and 750°C there were not relevant differences, in the 800°C and 850°C, instead, we can observe a deep precipitation of sigma phase which amount increase with the deformation.
In the following images sigma phase is shown with a white colour.

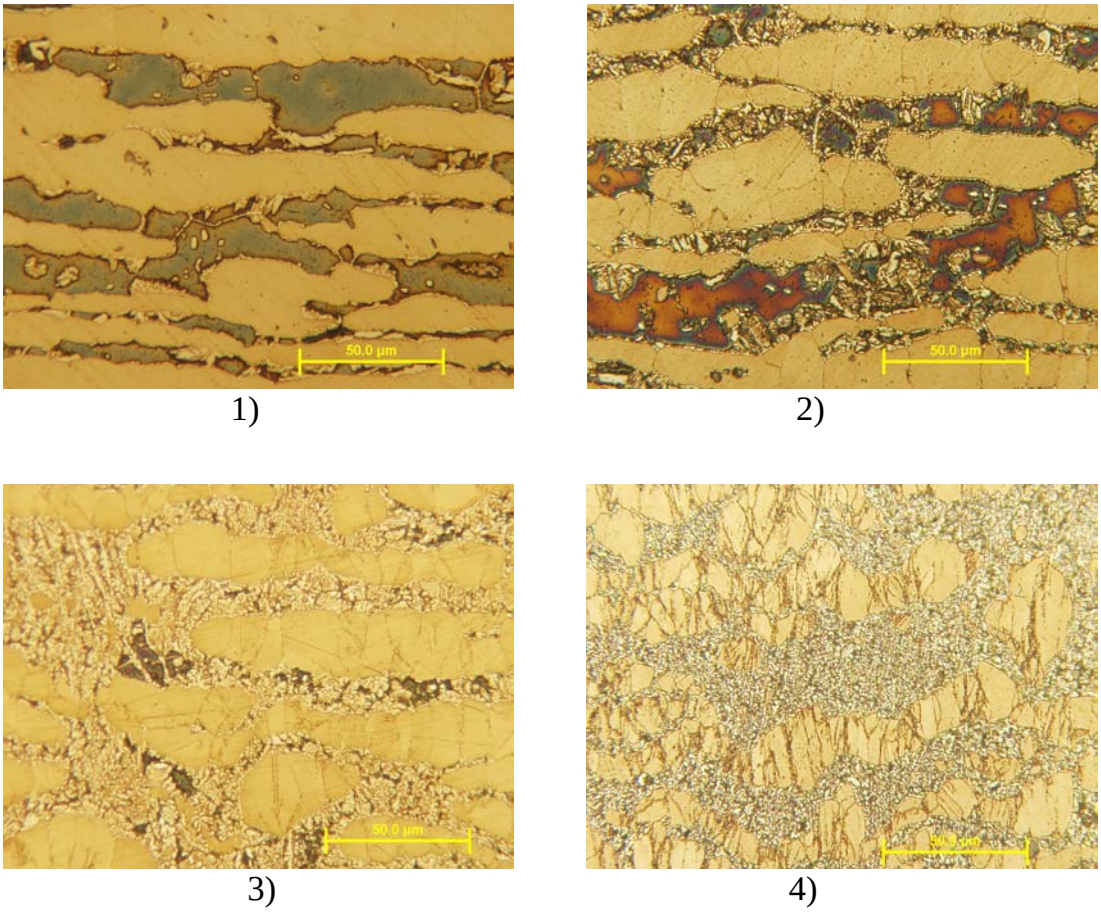

1) 2)

3) 4)

Fig 26. This 4 images are each one heat treated at 850°C for 1800s, in order
1) No deformation, 2) 20% deformation, 3) 40% deformation 4) 60% deformation

The sigma phase decomposition starts at grain boundaries 1), but some amount of sigma phase was found inside the austenitic grains 2).
Due to the increase of deformation, most of the ferrite decompose mainly into sigma phase and in the last two images 3) and 4) there is great difficulty to see ferrite grains.
In the next page the complete chart can be useful to understand the decomposition process.

3.2 EBSD RESULTS

The EBSD equipment is really useful because gives us much information about the sample such as phase ratio and grains orientation per each phase detected. The results from this technique are strongly dependent by the surface's condition: if the surface is not perfectly polished by silica clothing, the instrument can't analyse the sample properly because the Kikuchi lines[19] were difficult to detect giving a very low index factor.

We set the equipment with a step distance of 0.3μm between two points inside the selected area: this procedure took around 2 and 30 minutes to be completed. Due to the long estimated time we focus our attention in 6 out of 35 samples:

1	5	15	20	25	35
0% | 20°C	0% | 850°C	20% | 850°C	30% | 850°C	40% | 850°C	60% | 850°C

According to the magnetic test, the amount of sigma phase increases in the most deformed samples.

The images taken by the EBSD instrument were "cleaned up" by the software choosing 5px as grain size and 5° as degree grain tolerance. The phase map gives us the phase ratio directly and we can observe it in Tab 6.

Unfortunately the cleaning up process depends on the operators behaviour, and if the grains are particularly small it's possible to miss some information.

In Picture 1 we can see clearly just ferrite and austenite because the sample has not been deformed nor heat-treated. According to the previous results, in Picture from 2 to 4 we can see how increasing the deformation the amount of ferrite (red) decrease and decompose into sigma phase (yellow) and secondary austenite (green).

In the following images we can see the analysed phase map by EBSD:

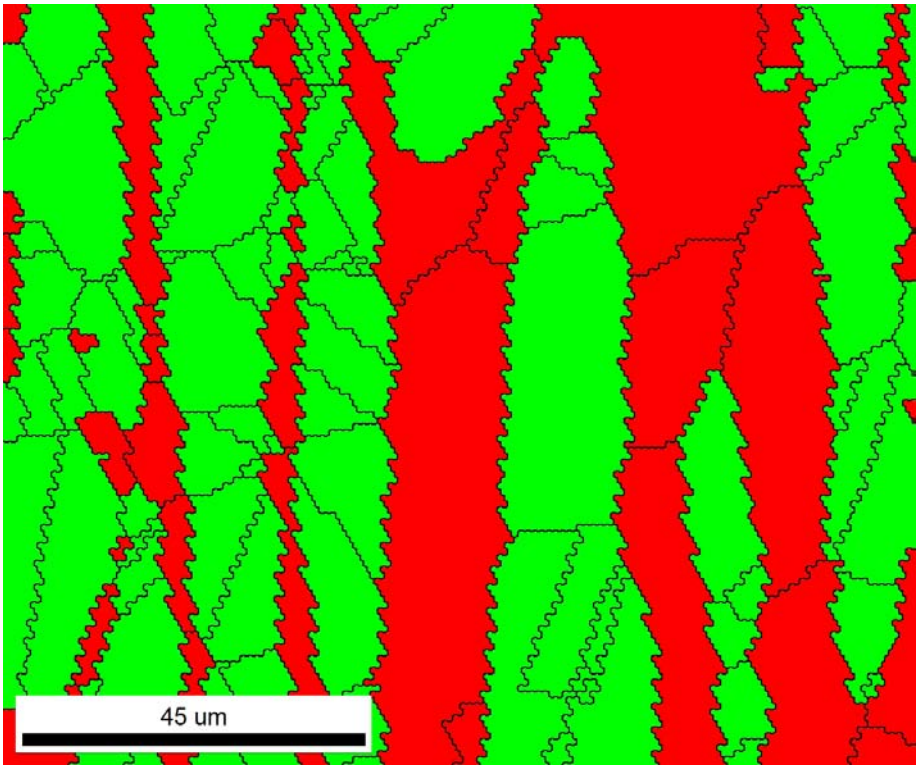

Picture 1. Base material, sample number 1

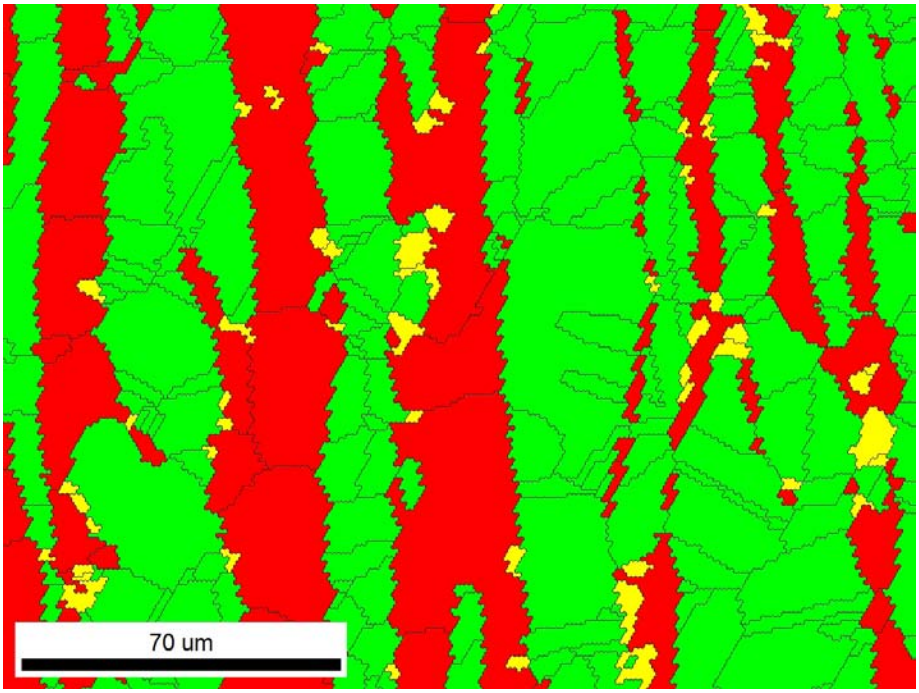

Picture 2. Sample number 5 heat treated at 850°C without deformation

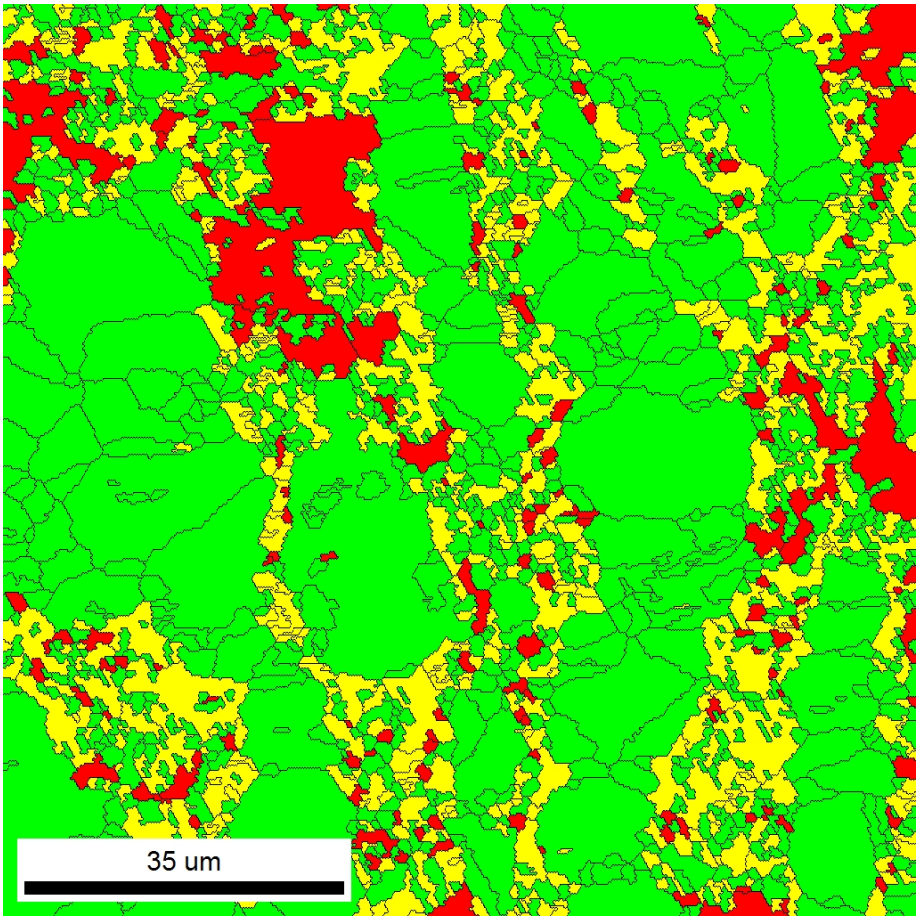

Picture 3. Sample number 25 (40% - 800°C)

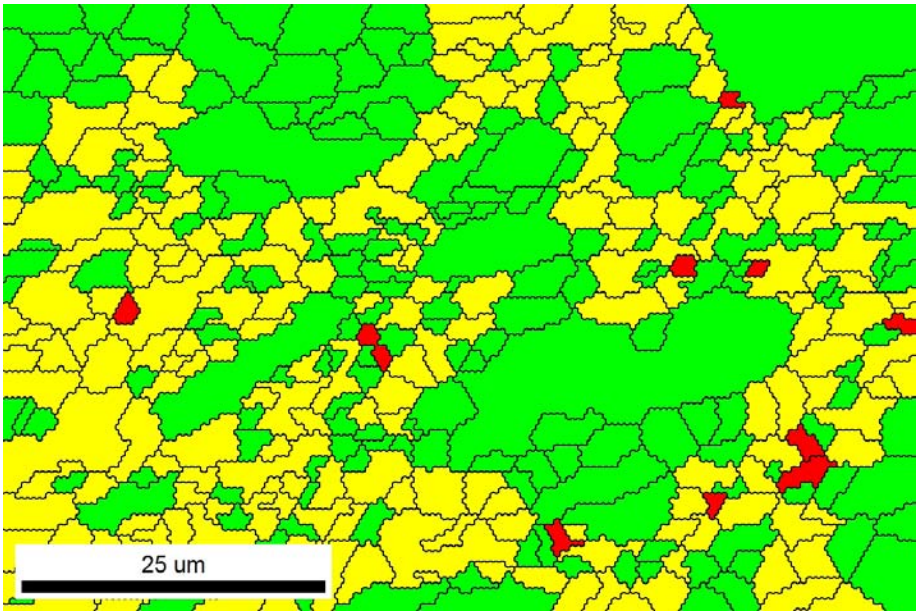

Picture 4. Sample number 35 (60% - 850°C)

In the following table we can see the trend of the sigma-phase with the deformation rate. The huge precipitation of sigma is substantial and in the last sample (number 35), most of ferrite has been decomposed.

The phase ratio can be observed in the following table:

SAMPLE	Ferrite	Austenite	Sigma-phase
1	41%	59%	0%
5	34,90%	57,60%	7,50%
15	33,20%	53,80%	13,00%
20	8,70%	72,90%	18,40%
25	9,80%	68,40%	21,80%
35	1,30%	52,30%	46,40%

Tab 6. Percentage of phase content in different sample with EBSD investigation

3.3 HARDNESS TEST

Hardness test has been performed for both austenite and ferrite phases but due to the instrument sensitivity data are not always accurate. Main reason is because in the most deformed samples precipitation of small particles of sigma phase along the grain boundaries increase the hardness and false the measurements.

Each hardness investigation has been taken 3 times and then an average value was calculated.

The instrument, KB Prüftechnik, was set up for 200g of load and 12 seconds of indentation time; as unit of measurement Vickers has been chosen.

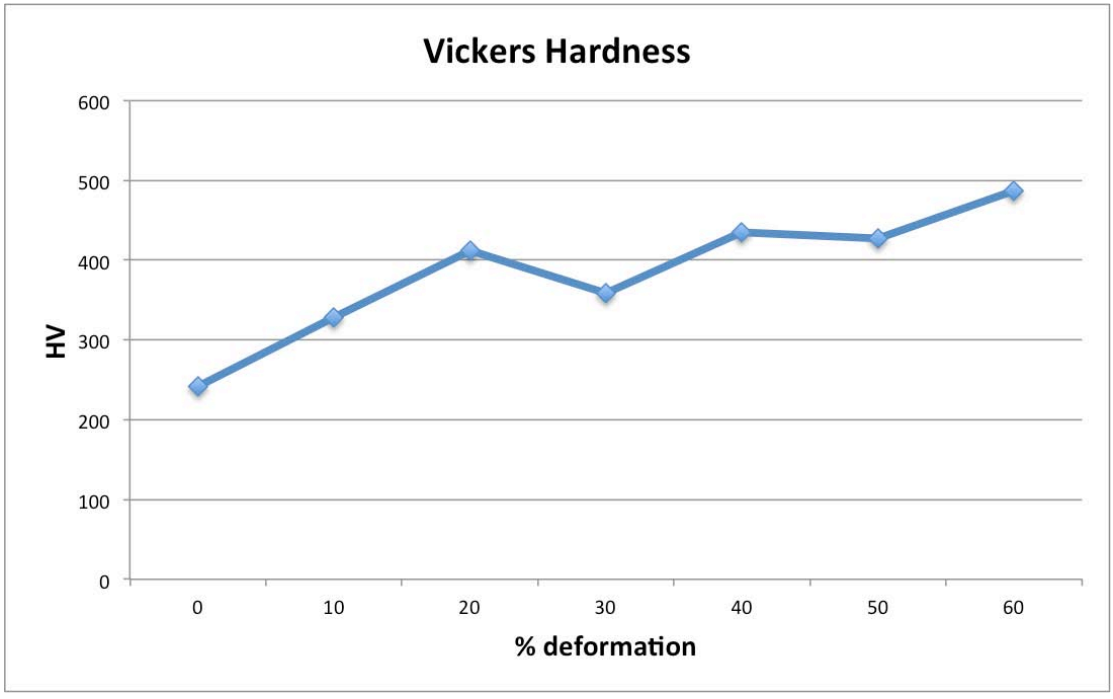

Fig 27. Average of hardness measurement at different thickness

As we can notice in Fig 27. hardness tends to increase with the increase of percentage reduction because new dislocation were created and starts moving due to the energy supplied by the deformation.

Stacking and blocking themselves, the dislocations increase their mechanical hardness, which is shown in the graph (Fig 27).

The information we got from this test is purely qualitatively because they are about the surface of the specimen and we cannot investigate inside the sample itself.

We also focused on hardness variation due to both the heat treatment and the thickness reduction and we the results can be seen in the Fig 28.

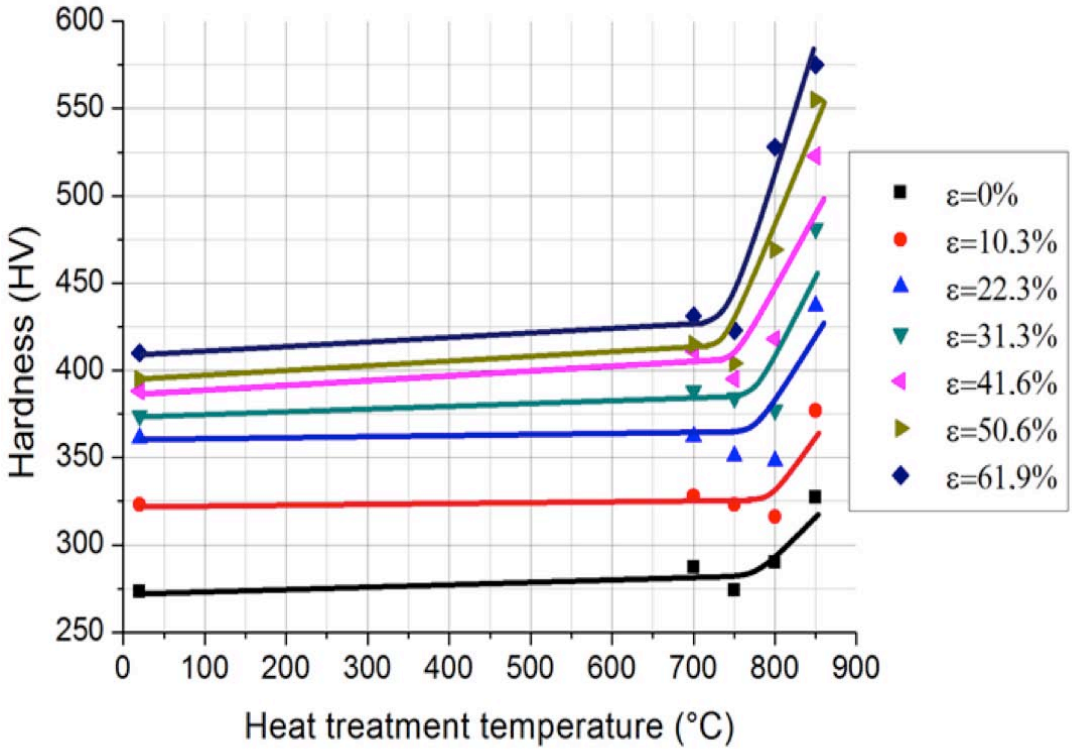

Fig 28. Hardness variation due to different heat treatment and deformation

As we can see, the hardness significantly increases in all samples starting from 750 °C. It is also possible to notice that the effect due to the deformation moves upwards the curves gradually due to deformation increase.

This increase over 750°C is due to the high amount of sigma phase precipitated in the samples, which is hard and brittle.

3.4 STÄBLEIN-STEINITZ TEST

In previous work on duplex stainless steel 2507[16], AC measurements test weren't able to supply an excitation field high enough to saturate 2507 DSS. That's the reason why we used DC measurements like Stäblein-Steinitz tester: it can reach over 3000A/cm, which is greater than AC measurement test.
In the following images we can see the hysteresis loop of deformed samples without heat treatment:

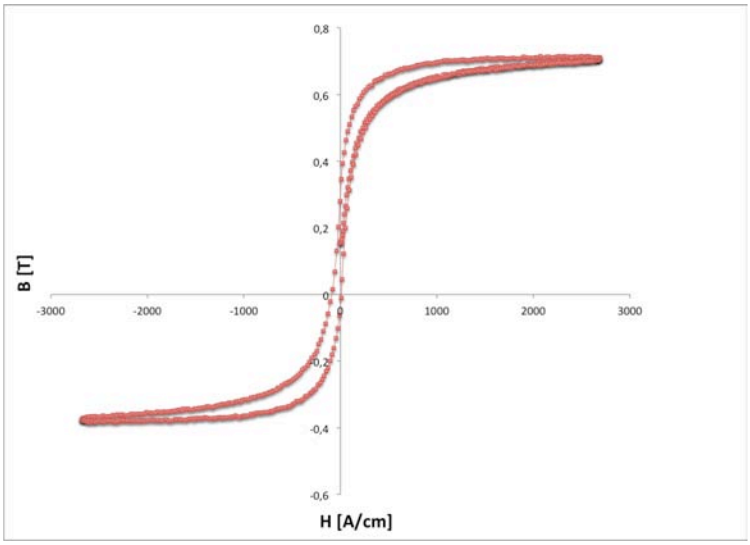

a)

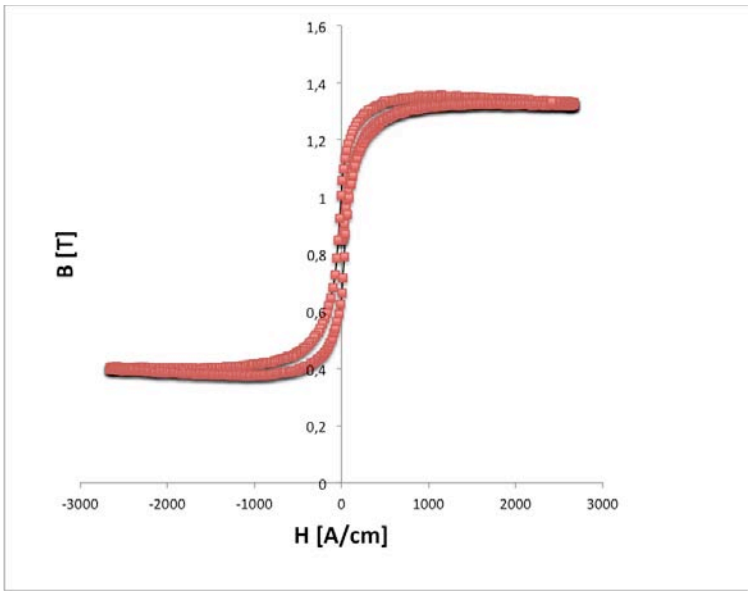

b)

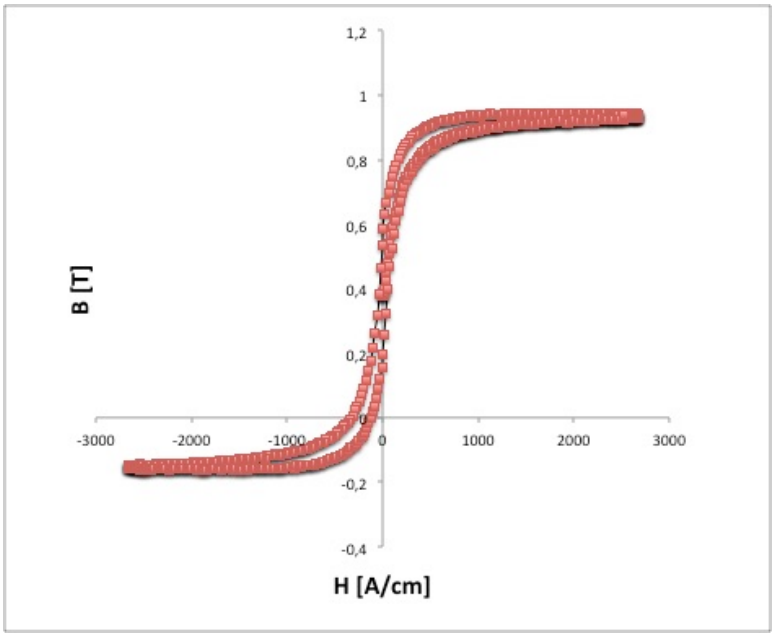

c)

Fig 29. Hysteresis loop of a) 0% thickness reduction b) 20% thickness reduction and c) 40% thickness reduction at room temperature

Although the curves do not have the same origin, the hysteresis curves are almost equal, and for this reason we have confirmation that the different thickness reduction do not influence the amount of ferromagnetic phase in the steel.

The shift of the curves from the origin is due to the device's calibration, which should be done for each samples making this measurements extremely long.

The Stäblein-Steinitz tester without samples should show an horizontal line, but it didn't happen due to error of the instrument so we analysed the "horizontal line" found out that the slope increase of the order of $1.2*10^{-5}$ and so we adjusted each curves with that factor.

Moreover we calculated for each graph the saturation polarization value B_{SP} subtract the minimum value of the loop to the maximum and divided the result by two.

$$B_{SP} = \frac{MAX - MIN}{2}$$

We put all the B_{SP} in a graph for a better comprehension:

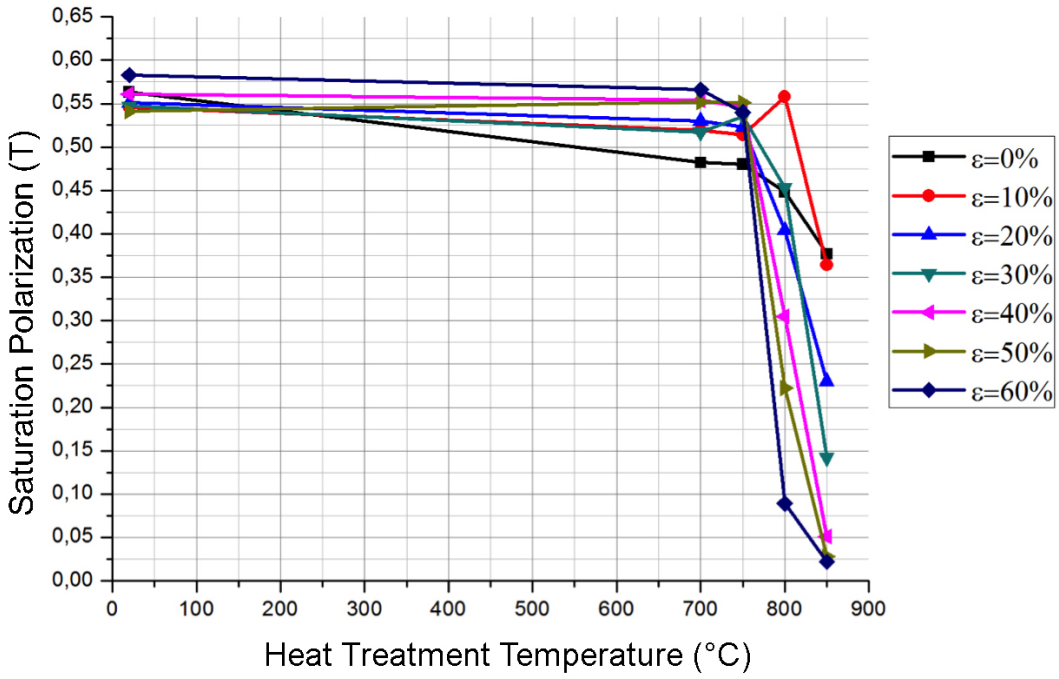

Fig 30. Saturation polarization diagram for each thickness reduction

The graph in Fig 30 shows the trend of the saturation polarization value. Except for one point in 10% thickness reduction sample at 800°C which is due to operator or instrument error, others show a decrease in heat treated samples at temperature higher than 750°C.

In this samples the amount of ferromagnetic phase, so called ferrite, is extremely low due to the decomposition process into sigma phase and secondary austenite, this is the reason why the saturation polarization value decreased.

More deformed is the specimen, lower is the ferrite content and lower is the saturation polarization value.

3.5 EDDY-CURRENT TEST

Each specimen has been measured at 4 different frequencies: 10kHz – 40kHz – 66,7kHz – 100kHz.

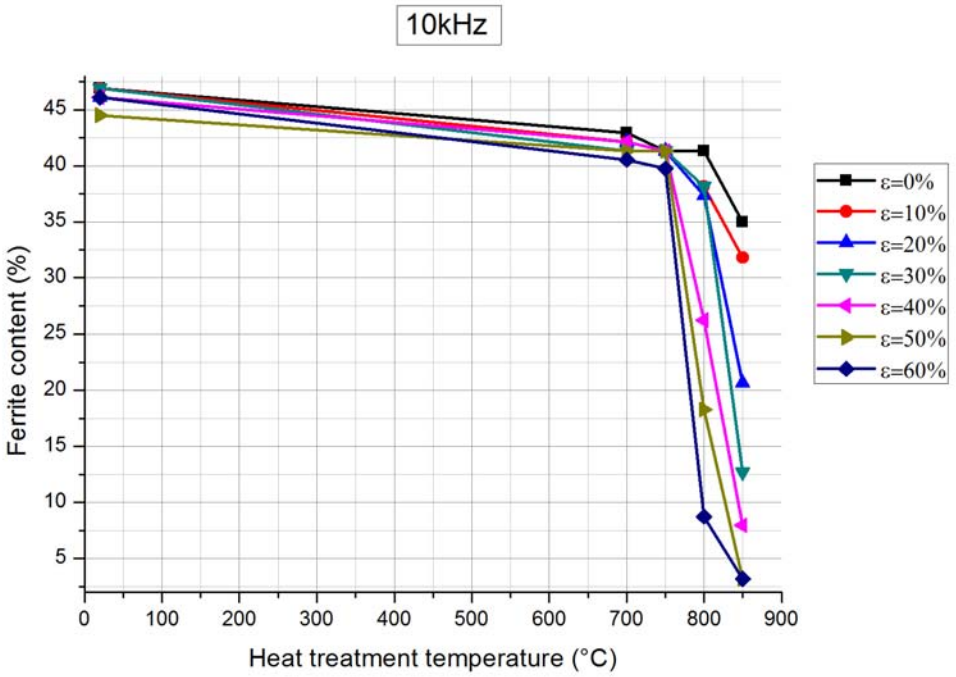

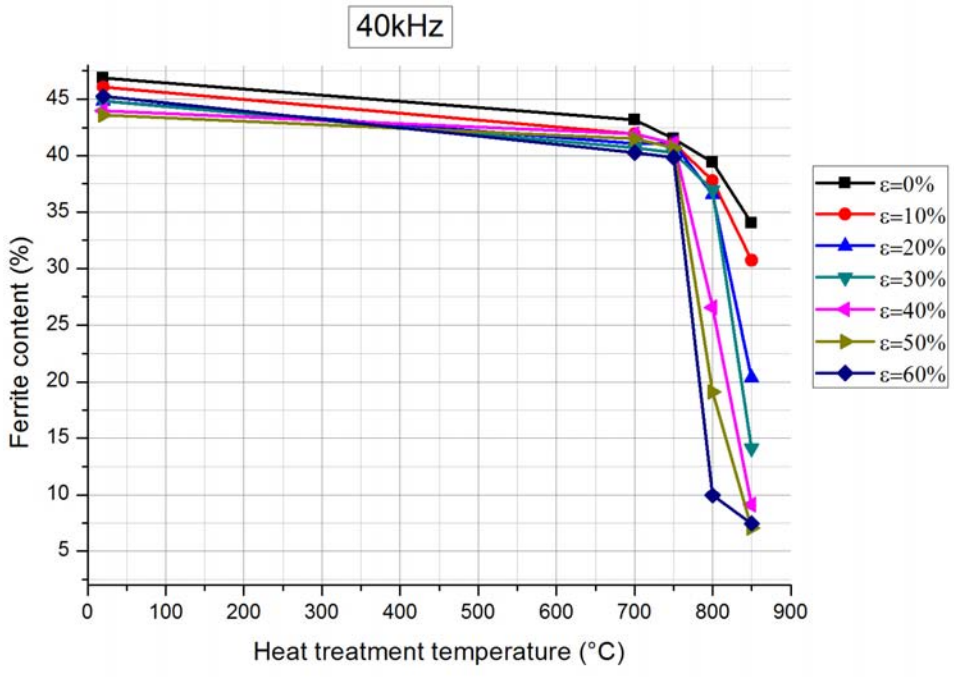

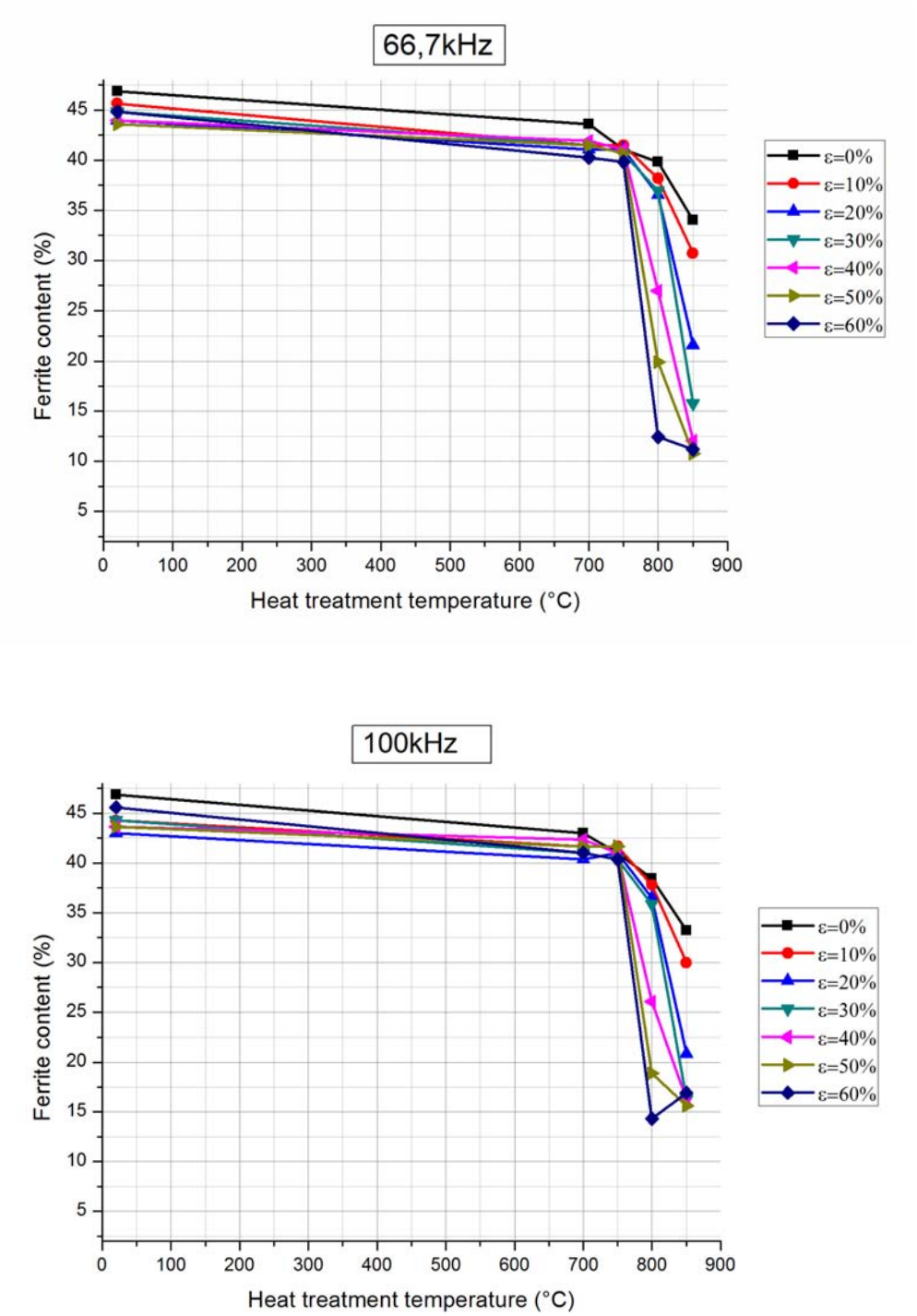

Fig 31. 4 frequencies diagrams of Eddy-Current test

The four graphs show the amount of ferrite calculated at different frequencies, we notice that the 10kHz measurement is the most accurate ones according to the EBSD results.

3.6 FISCHER-FERRITE TEST

Before the test all samples has been polished by 320P to remove every possible oxide substrate on the surface, which would distort the measurements.
The measures were taken for each face of the specimen and in the following table the data is an average of 4 measurements of the same face.

T (°C)	e=0%	e=10%	e=20%	e=30%	e=40%	e=50%	e=60%
20	47,4	45,7	42,5	42,1	41	39,7	38,9
700	41,2	38,7	38,2	37,2	39,1	37,4	35
750	37,6	37	36,9	37	37,3	35,3	34,4
800	35,4	33,4	32,5	31,1	22,3	13,7	7,8
850	27,8	25,4	15,7	9,3	5,5	2,6	1,4

Tab 7. Ferrite percentage measured with Fischer feritscope

For a better analysis we had inserted all the data collected into a graph:

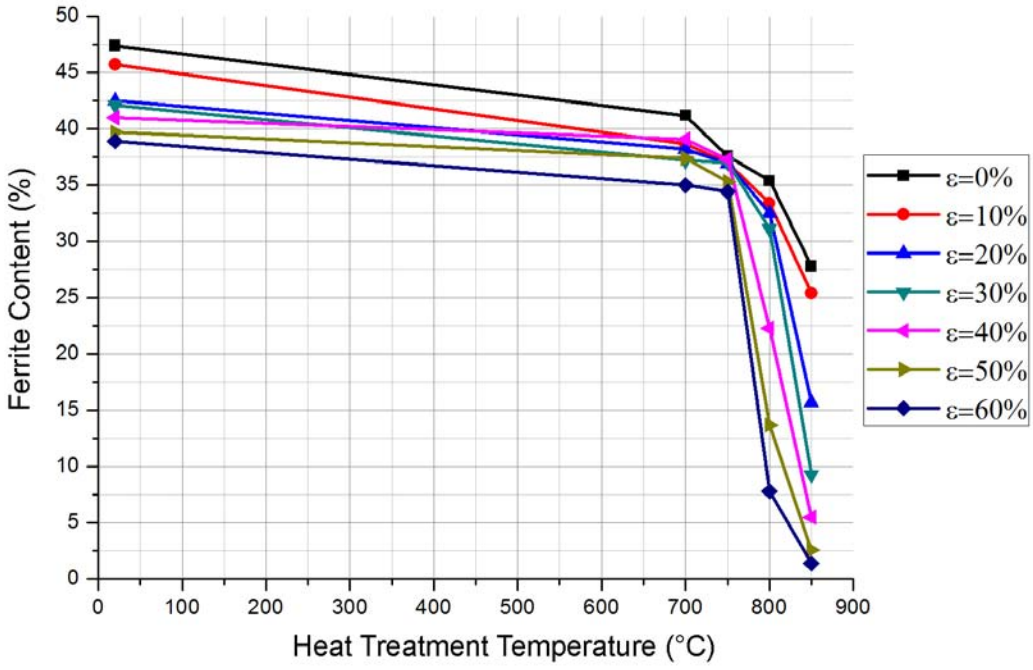

Fig 32. Ferrite content calculated with Fischer-Feritscope at different heat treated samples

We can observe that, according to the Eddy-Current and Stäblein-Steinitz test, the amount of ferrite decrease with heat treatment over 750°C.

3.7 X-RAY DIFFRACTION TEST

Samples were investigated in the Metallurgy Institute at University of Miskolc. Tab 8 shows those samples which have been investigated by X-ray diffraction.

Sample number	Deformation rate (%)	Heat Treatment Temperature (°C)	Fig.
1	0	20	1,2,6
3	0	750	2,3
5	0	850	2,5
20	30	850	5
33	60	750	3,4
35	60	850	1,4,7

Tab 8. Investigated samples by XRD

The diffractograms were created by a D8 Advanced diffractrometer with copper X-ray radiation. Qualitative phase analysis was made by Bruker EVA software and was determined by APX63 software. Two samples out of 6 were measured in parallel with Göbel mirror and Bruker D8 Advanced equipment (which contained a position sensitive detector) in the Mineralogy Institute at the University Of Miskolc. Rietveld method and Bruker Topas software were used on the diffractograms to determine the amount of the phases. Unfortunately the results obtained by APX63 software are completely wrong and they were not included in this thesis.

At least 3 reflections of a phase need for the program to calculate the content amount of the phase. If there is less reflection the matrix, which is necessary for the calculation, cannot exist.

Sample number	**Deformation rate (%)**	**Heat Treatment Temperature (°C)**	**Ferrite (%)**	**Austenite (%)**	**Sigma (%)**
1	0	20	42.31	57.69	-
35	60	850	-	54.45	45.55

Tab 10. Ferrite, Austenite and Sigma percentage results with Rietveld method

We noticed that there are differences between the Rietveld method results (Tab 10) and the other results (Tab 9).
The possible reasons of this differences:

- The texture of the sample, for example: in sample 1, the orientation which was considered by the ferrite first refection could not be used by the second reflection
- There is no proper crystallography information about the dissolved Cr atoms in case of the sigma-FeCr phase: in sample 35, 5% Cr was supposed but if the solubility is higher it can cause significant changes.

For this reason we do not take into consideration the results from Tab 9. and we analysed only results from Tab 10.
The Fig 33 shows the diffractogram of sample 1, which contained only ferrite and austenite.

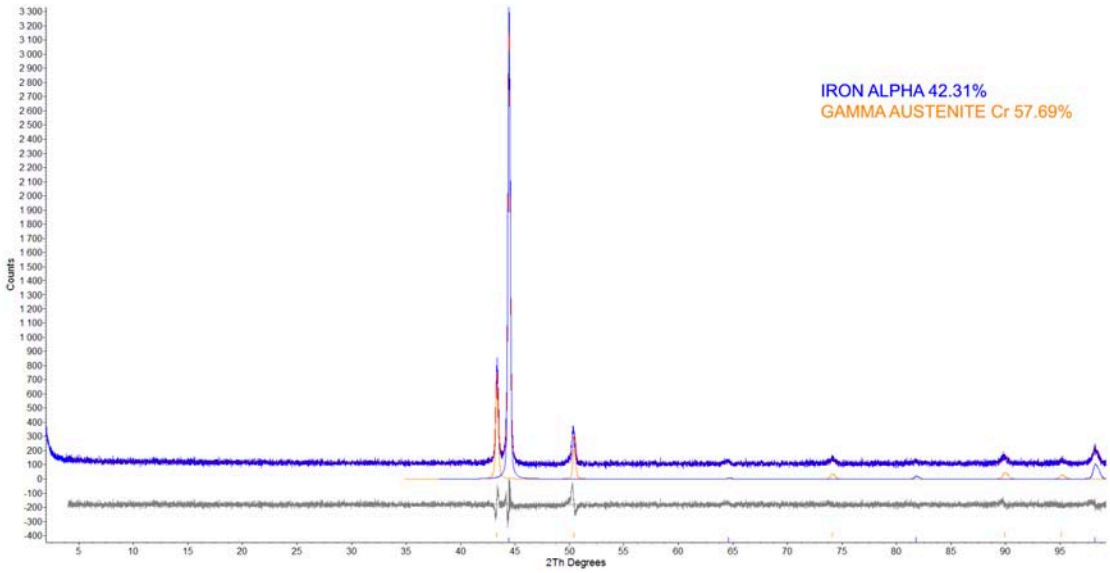

Fig 33. Diffractogram of sample 1, blue curve is ferrite content, orange curve is austenite

The sample number 35, which was 60% cold rolled and heat treated at 850°C, contained largely austenite and sigma phase and can be confirmed by Fig 34.

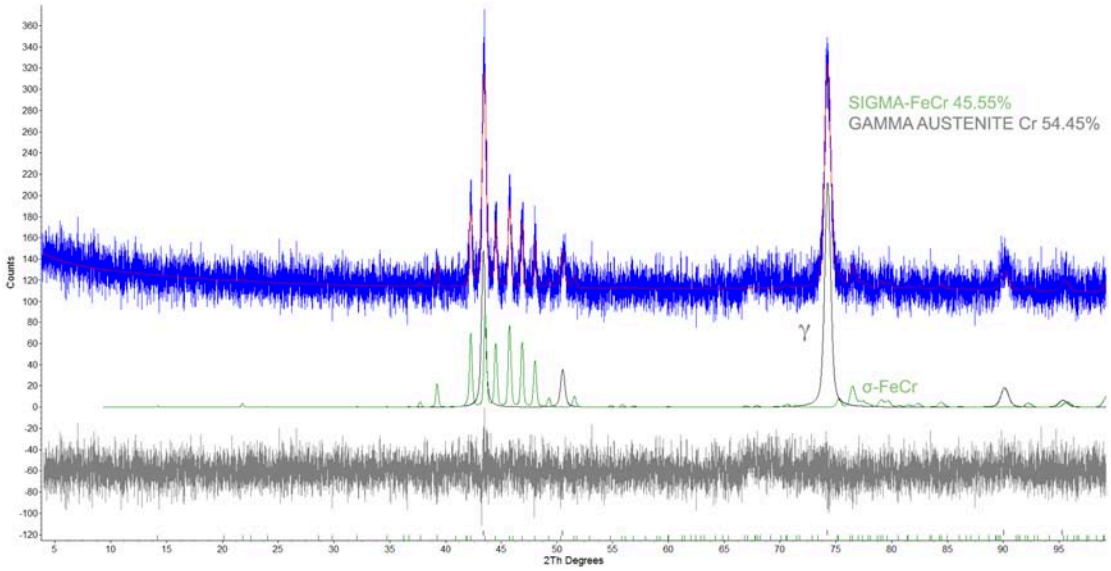

Fig 34. Diffractogram of sample 35, green curve is sigma content, grey curve is austenite

According to EBSD results, the Rietveld method results are quite good. Unfortunately this test takes from 7 to 8 hours to be completed for one sample and only two samples had been evaluated.

3.8 DENSITY TEST RESULTS

All density measurements have been taken by AccuPyc II 1340 Pycnometer. Every measurement took about 50 minutes, because the instrument performed 10 cycles: each cycle is equal to 1 density measurement. In the following chart the value is an average between the 10 cycles measured.

Sample	Mass (g)	Standard Deviation (g/cm^3)	Density (g/cm^3)
1	6,52	0,0037	7,7434
2	6,44	0,0044	7,7345
3	6,37	0,0242	7,7768
4	6,55	0,0065	7,7779
5	6,54	0,008	7,7963
6	6,55	0,0085	7,7598
7	6,45	0,0064	7,7561
8	6,46	0,0038	7,7634
9	6,47	0,0053	7,7611
10	6,47	0,0057	7,7778
26	6,51	0,0088	7,7575
27	6,63	0,006	7,7361
28	6,62	0,0049	7,7387
29	6,42	0,0072	7,7869
30	6,52	0,0042	7,7731
31	5,88	0,007	7,7348
32	6,33	0,0084	7,7409
33	6,37	0,0057	7,7439
34	6,26	0,004	7,7757
35	6,5	0,0079	7,801

Tab 11. Average values from AccuPyc II 1340 Pycnometer

For a better understanding, we have plotted the data obtained from the density tests diagram Fig 35: we noticed that there is an increase in density in the heat treated specimens due to the decomposition from ferrite to austenite.
Unfortunately, as we can noticed in Fig 35. Sample number 30 measurement is incorrect probably due to instrument or operator errors.
Anyway we cannot say nothing regarding the deformation because there is not a relation between density and deformation rate.

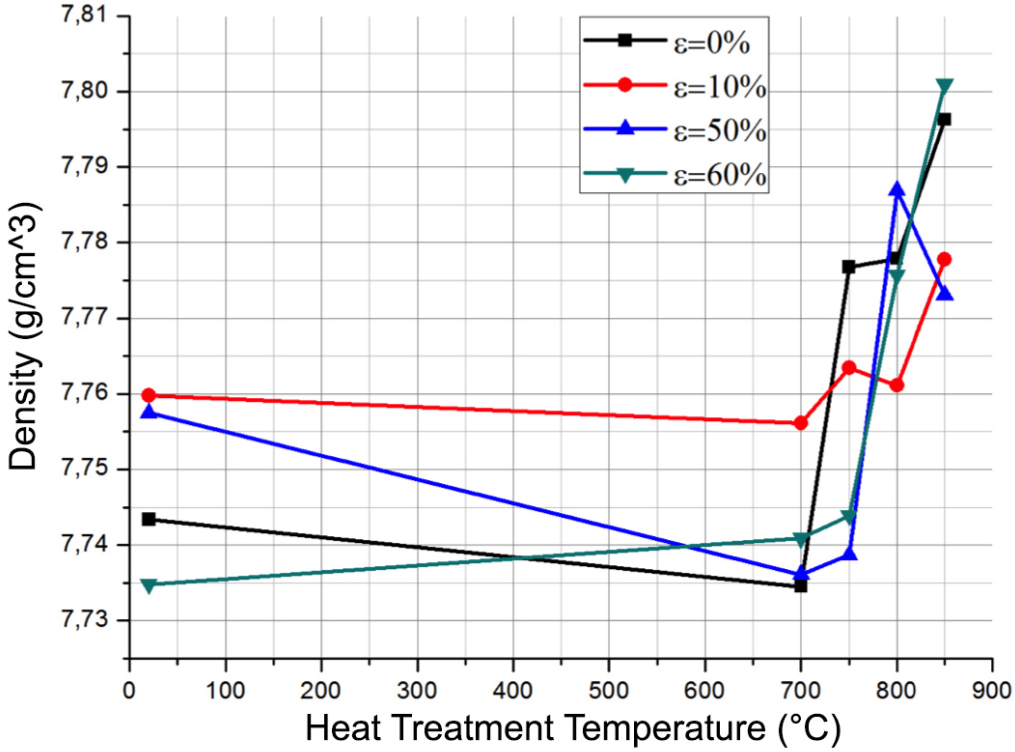

Fig 35. Density test data plotted in a graph

3.9 CORROSION TEST RESULTS

After 24h all samples had been cleaned from ferric chloride and weighed, and this procedure has been repeated after 48h and 72h.

First of all, the specimens with the highest heat treatment were heavily damaged and this can be observed easily to the naked eye.

A table with all the masses before and after the 24h, 48h and 72h had been prepared (Tab 12) and after that a graph had been plotted to analyzed the mass variations of the samples.

	Original mass (g)	Mass after 24h (g)	Mass after 48h (g)	Mass after 72h (g)	Mass reduction after 72h (g)	Mass reduction after 72 h (%)
1	6,518	6,5176	6,5175	6,5170	0,0010	0,015342129
2	6,4373	6,4365	6,4363	6,4361	0,0012	0,018641356
3	6,3644	6,3639	6,363	6,3626	0,0018	0,02828232
4	6,5302	6,5254	6,5219	6,5078	0,0224	0,343021653
5	6,5208	6,4462	6,4406	6,4397	0,0811	1,243712428
6	6,5396	6,5395	6,5395	6,5395	0,0001	0,001529146
7	6,4271	6,4262	6,4258	6,4248	0,0023	0,035785969
8	6,438	6,4375	6,4369	6,4365	0,0015	0,023299161
9	6,4648	6,464	6,4631	6,4627	0,0021	0,032483604
10	6,4468	6,4208	6,4168	6,4139	0,0329	0,510330707
11	6,1098	6,1096	6,1083	6,1083	0,0015	0,024550722
12	5,9583	5,9582	5,9582	5,958	0,0003	0,005034993
13	6,6411	6,6405	6,6402	6,6399	0,0012	0,018069296
14	6,5735	6,5707	6,5694	6,5678	0,0057	0,086711797
15	6,4182	6,2442	6,2298	6,2268	0,1914	2,982144527
16	6,2033	6,2032	6,2031	6,203	0,0003	0,004836136
17	6,3423	6,3421	6,342	6,3409	0,0014	0,022074011
18	6,6548	6,6538	6,6535	6,6535	0,0013	0,019534772
19	6,4051	6,3867	6,3784	6,377	0,0281	0,438712901
20	6,4373	6,3139	6,2434	6,223	0,2143	3,329035465
21	6,4936	6,4933	6,4931	6,493	0,0006	0,009239867
22	6,373	6,3729	6,3728	6,3728	0,0002	0,003138239
23	6,6259	6,6257	6,6255	6,6252	0,0007	0,010564603
24	6,4919	6,2448	6,163	6,1525	0,3394	5,22805342
25	6,7338	6,5045	6,4163	6,3977	0,3361	4,991238231
26	6,495	6,4949	6,494	6,4938	0,0012	0,018475751
27	6,6284	6,628	6,627	6,6269	0,0015	0,022629896
28	6,614	6,6138	6,6137	6,6135	0,0005	0,007559722
29	6,3945	6,0665	6,0152	5,9998	0,3947	6,172491985
30	6,5252	6,239	6,1482	6,1368	0,3884	5,952307975
31	5,8656	5,8655	5,8654	5,8654	0,0002	0,003409711
32	6,3095	6,3089	6,3082	6,3081	0,0014	0,022188763
33	6,3584	6,358	6,3579	6,3578	0,0006	0,009436336
34	6,255	6,0244	5,9924	5,9582	0,2968	4,745003997
35	6,4799	6,3205	6,258	6,2448	0,2351	3,62814241

Tab 12. Mass reduction after 24h, 48h and 72h

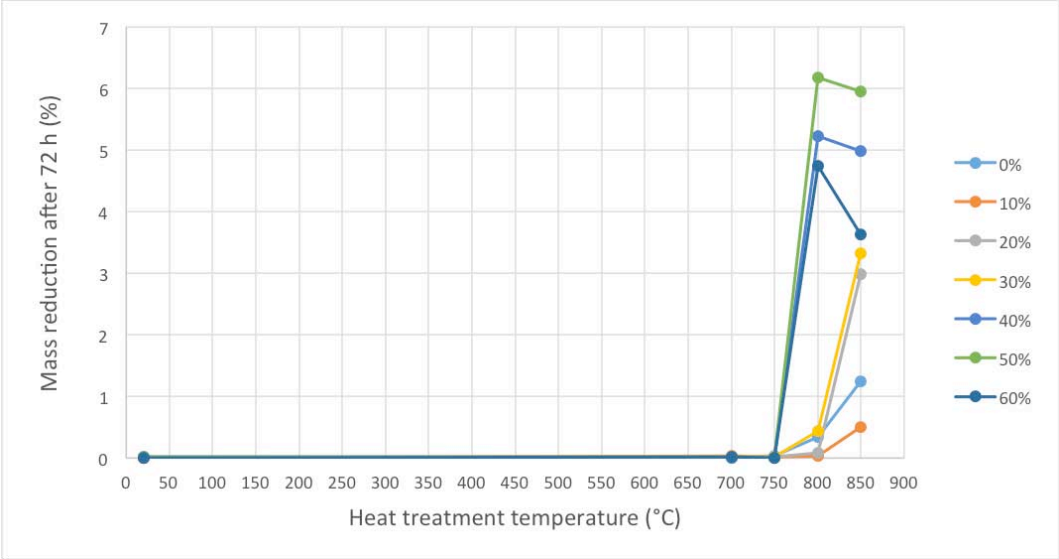

Fig 36. Mass reduction after 72h

Looking at Fig 36, we can say that under 750°C the mass reduction is very low, practically we can't see a reduction, because the ferrite phase didn't transform into sigma phase and secondary austenite. The corrosion resistance decrease above 750°C, due to the decomposition of ferrite and this results are similar to the DC magnetometer results, because the mass reduction starts where the eutectoid decomposition begins (which is over 750°C).

We also counted the number of pittings, which were formed at the end of each corrosion cycle. But there isn't a correlation between the pitting number and the deformation.

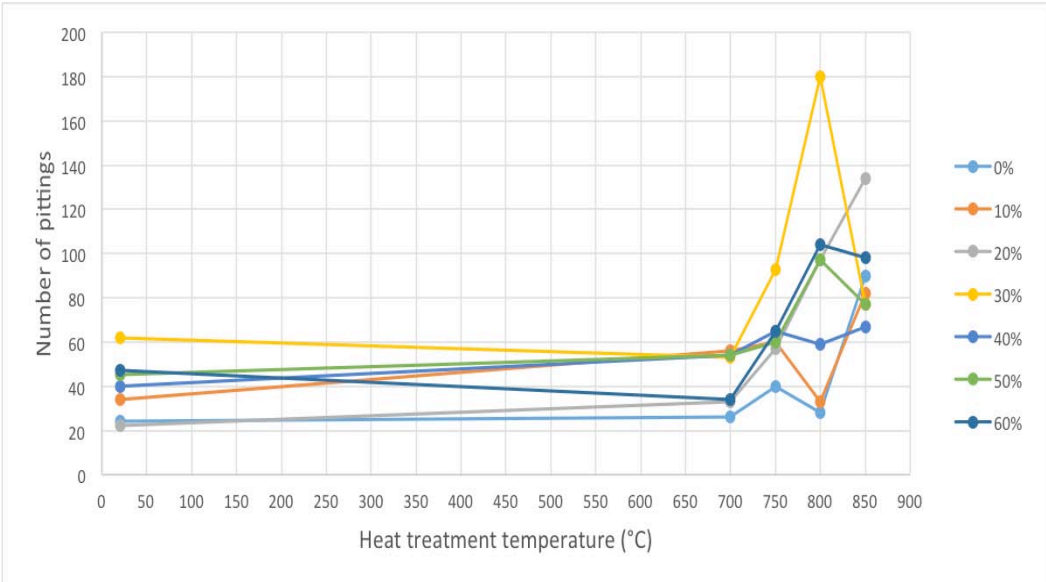

Fig 37. Number of pittings after 72h

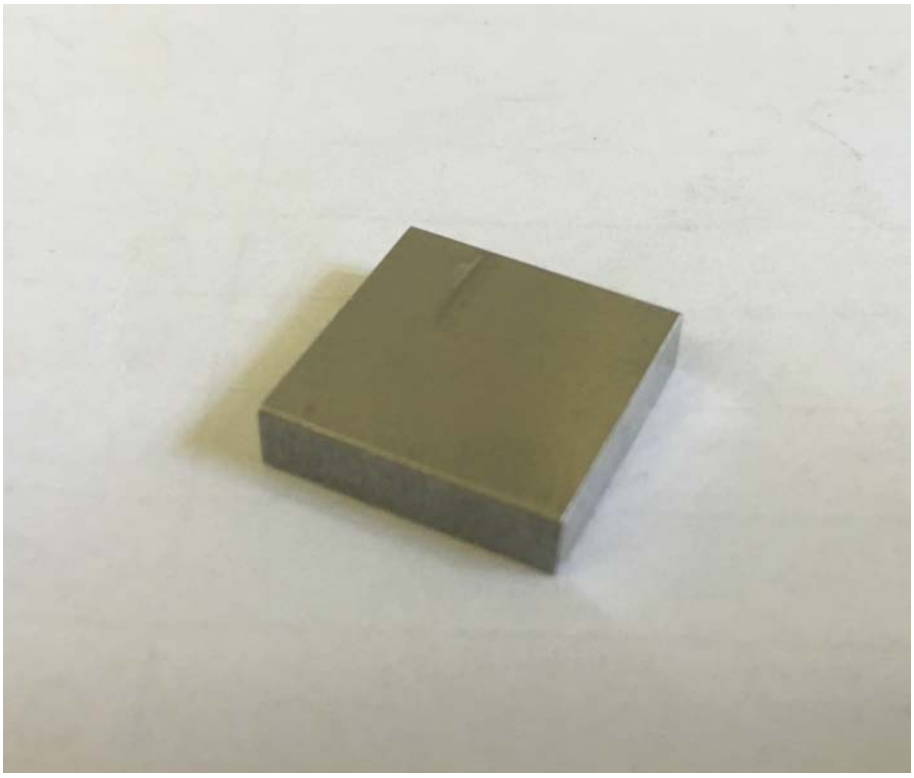

Fig 38. Sample number 29 before the corrosion test.

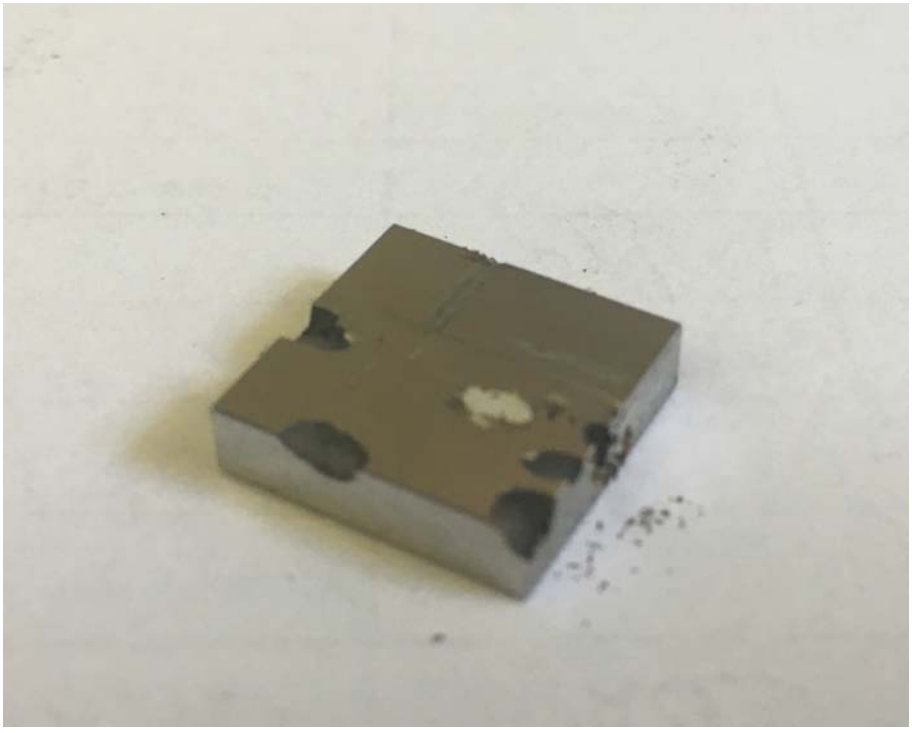

Fig 39. Sample number 29 after 72h into $FeCl_3$

CONCLUSIONS

The DSS 2507 type was investigated by different magnetic tests like Stäblein-Steinitz. Eddy-Current and Fischer ferrite but also with non-destructive tests like EBSD and Density test and destructive tests like hardness and corrosion test.

We analysed the decomposition process of δ-ferrite phase due to heat treatment and cold rolling deformation and see the relation between them in the process.

We noticed that:

- The phase transformation starts between the range of 700°C and 750°C and, according to the tests, the rate of the phase transformation increases with the deformation.

- In the non deformed samples (1 to 5) the phase transformation starts at the grain boundaries, in the deformed samples the decomposition occurs inside the grain boundaries as well.

- The σ-phase precipitation is enhanced by the plastic deformation, and in the most deformed sample (50% and 60%) the ferrite had almost completely disappeared.

- Hardness test shows that hardness increase due to plastic deformation. At 800°C, in strongly deformed samples, the increase of σ-phase amount leads to an increase of hardness.

- As noticed in the density test, between 700°C-750°C there is an increase of specific density of the alloy due to the reduction of ferrite (lower density) compared to austenite (higher density).

- Analysing the corrosion test we can confirm that the optimal ratio of ferrite and austenite in DSS for the best corrosion resistance is 45% ferrite and 55% austenite: if the amount of ferrite decrease even just 5% corrosion has detected.

REFERENCE:

[1] E.C. Bain, W.E. Griffith, Trans AIME, 75 (1927) 166.

[2] R.N. Gunn, Duplex Stainless Steels: Microstructure, properties and applications. Ed.

[3] I. Alvarez-Armas, Duplex Stainless Steels: Brief History and Some Recent Alloys, Recent Patents on Mechanical Engineering, 1 (2008) 51-57.

[4] Giovanni Fassina, Effects of cold rolling on austenite to α ’ - martensite transformation in 2101 lean duplex stainless steel, Msc work, 2010.

[5] R.N. Gunn, Duplex Stainless Steels: Microstructure, properties and applications. Ed.

[6] I. Alvarez-Armas, Duplex Stainless Steels: Brief History and Some Recent Alloys, Recent Patents on Mechanical Engineering, 1 (2008) 51-57.

[7] D.S. Bergstrom, Benchmarking of Duplex Stainless Steels versus Conventional Stainless Steel Grades, Proc. 7th Duplex 2007 Int. Conf & Expo, Grado, Italy (2007).

[8] J. Olsson, M. Snis, Duplex - A new generation of stainless steels for desalination plants. Desalination, 205 (2007) 1-3: 104-113.

[9] Manfrin, Effetto della deformazione a freddo sulle trasformazioni di fase per l’acciaio SAF2507 indotte da trattamento termico, Msc work, 2011.

[10] Bela Leffler, Stainless steels and their properties, Outokumpu publication.

[11] Gomes de Abreu, Santana de Carvalho, de Lima Neto, Pires dos Santos, Nogueira Freire, de oliveira silva, souto mario tavares. Deformation Induced Martensite in an AISI 301LN Stainless Steel: Characterization and Influence on Pitting Corrosion Resistance, Materials Research, Vol. 10, No. 4, (2007) pp 359-366.

[12] Weisbrodt-Reisch, Brummer, Hadler, Wolbank, Werner, Influence of

temperature, cold deformation and a constant mechanical load on the microstructural stability of a nitrogen alloyed duplex stainless steel. Materials Science and Engineering A 416 (2006) pp 1–10.

[13] Hadji, Badji, Microstructure and Mechanical Properties of Austenitic Stainless Steels After Cold Rolling, JMEPEG (2002) 11 pp 145-151.

[14] Stablein, F. – Steinitz, R.: Ein Neuer Doppeljoch Magnetstalprüfer, Archiv für das Eisenhüttenwesen 8, (1935), 549-554.

[15] I. Mészáros, Testing of stainless steel by double yoke DC magnetometer Journal of electrical engineering, VOL 61. NO 7/s, 2010, 62-65

[16] Bianchi M. Effects of cold rolling on phase precipitation and phase transformation in a 2507 SDSS Msc work (2011)

[17] ANSI/ASTM G48 Pitting and crevice corrosion resistance of stainless steels and related alloys by the use of ferric chloride solution, 1976

[18] D O'Sullivan, M Cotterell, D A Tanner, I Mészáros: Characterisation of ferritic stainless steel by Barkhausen techniques, NONDESTRUCT TEST EVA 37: 489-496 (2004)

[19] Tibor Berecz, István Mészáros: Studying of Microstructural Effects of Surface Rolling in Materials of Railway-car Wheel Axles by EBSD and NDT Magnetic Measurement, MATER SCI FORUM **729**: 308-313 (2013)

[20] I Calliari, M Breda, E Ramous, I Mészáros: Phase transformations in duplex stainless steels: Metallographic and magnetic investigation, YEJIN FENXI **33**: (7) 10-15 (2013)

[21] S Baldo, I Mészáros: Effect of cold rolling on microstructure and magnetic properties in a metastable lean duplex stainless steel, J MATER SCI **45**: 5339-5346 (2010)

[22] M Breda, L Pezzato, M Pizzo, I Mészáros, I Calliari: Effects of Cold Deformation in Duplex Stainless Steels, In: EUROMAT 2013.

[23] Weisbrodt-Reisch, Brummer, Hadler, Wolbank, Werner, Influence of temperature, cold deformation and a constant mechanical load on the microstructural stability of a nitrogen alloyed duplex stainless steel. Materials Science and Engineering A 416 (2006) pp 1–10.

[24] Maitlan, Sitzman, Electron Backscatter Diffraction (EBSD) Technique and Materials Characterization Examples, Scanning microscopy for nanotechnology techniques and applications (2007) pp 41-75.

[25] Tibor Berecz, István Mészáros, Péter János Szabó: Decomposition of the Ferritic Phase in Isothermally Aged SAF 2507 Duplex Stainless Steel, MATER SCI FORUM **589**: 185-190 (2008)

[26] I Mészáros: Magnetic characterisation of duplex stainless steel, PHYSICA B **372**: 181-184 (2006)

[27] S Baldo, M Zanelatto, I Mészáros: Phase transformation in 2101 DSS after cold rolling, In: DUPLEX Stainless Steels 2010: DUPLEX 2010 AIME, 2010. pp. 10 (Konferenciaközlemény)

[28] B. Bögre, I. Mészáros – Study of ferrite decomposition in duplex stainless steel Volume 66, 2015. December ISSN 1335-3632 (4 oldalas cikk)

[29] https://en.wikipedia.org/wiki/X-ray_crystallography

[30] http://www.electronics-tutorials.ws/electromagnetism/

[31] http://www.helmut-fischer.ch/

[32] http://www.rmki.kfki.hu/

[33] http://www.olympus-ims.com/en/eddycurrenttesting/